ARTICLE

doi:10.1038/nature26159

The logic of single-cell projections from visual cortex

Yunyun Han[1,2,3]*, Justus M. Kebschull[4,5]*, Robert A. A. Campbell[3]*, Devon Cowan[3], Fabia Imhof[3], Anthony M. Zador[5]§ & Thomas D. Mrsic-Flogel[3,6]§

Neocortical areas communicate through extensive axonal projections, but the logic of information transfer remains poorly understood, because the projections of individual neurons have not been systematically characterized. It is not known whether individual neurons send projections only to single cortical areas or distribute signals across multiple targets. Here we determine the projection patterns of 591 individual neurons in the mouse primary visual cortex using whole-brain fluorescence-based axonal tracing and high-throughput DNA sequencing of genetically barcoded neurons (MAPseq). Projections were highly diverse and divergent, collectively targeting at least 18 cortical and subcortical areas. Most neurons targeted multiple cortical areas, often in non-random combinations, suggesting that sub-classes of intracortical projection neurons exist. Our results indicate that the dominant mode of intracortical information transfer is not based on 'one neuron–one target area' mapping. Instead, signals carried by individual cortical neurons are shared across subsets of target areas, and thus concurrently contribute to multiple functional pathways.

While the inputs received by a neuron drive its activity, its axonal projections determine its effects on other neurons. The axons of excitatory projection neurons that reside in layers 2 and 3 (hereafter 2/3), and 5 and 6 of the neocortex are the main conduit by which signals are exchanged between cortical areas[1]. To date, no study has, to our knowledge, systematically investigated the principles by which individual neurons in any region of the mammalian neocortex distribute information to their targets. This knowledge is fundamental for deducing the logic of the communication between areas, for constraining hypotheses about neural function and for the identification of putative sub-classes of neurons. Anatomical studies in macaques, cats and mice, which are mostly based on retrograde tracing methods, indicate that there is an abundance of intracortical projection neurons in the sensory neocortex, which have axons that appear to innervate single target areas[2–6], raising the possibility that information may be distributed through ensembles of dedicated pathways that are functionally tailored to each target[6–12]. For example, neurons in the mouse primary visual cortex (V1) that innervate the posteromedial (PM) or anterolateral (AL) area appear to match the spatial and temporal frequency preference of these target areas[7,13,14]. Similarly, neurons in the mouse primary somatosensory cortex that project to either the primary motor cortex or the secondary somatosensory area comprise largely non-overlapping populations with distinct physiological and functional properties[6,9,10]. These findings indicate that dedicated lines—specialized subpopulations of neurons that preferentially target a single downstream area (Fig. 1a, left)—may represent a fundamental mode of cortico-cortical communication. Alternatively, intracortically projection neurons could broadcast to multiple targets[4,5,15–19], either randomly (Fig. 1a, middle) or by targeting specific sets of areas (Fig. 1a, right). These three models of cortical architecture have different implications for communication between areas underlying sensory processing in hierarchical networks. To distinguish between these models, we used two anterograde anatomical approaches, whole-brain fluorescence-based axonal tracing and high-throughput DNA sequencing of genetically barcoded neurons (MAPseq), to map the long-range axonal projection patterns of individual neurons in the mouse primary visual cortex, an area that distributes visual information to multiple cortical and subcortical targets[20–22].

Fluorescence-based tracing of single neurons

We first traced the projections of single neurons using whole-brain fluorescence-based axonal reconstructions. We used single-cell electroporation of a GFP-encoding plasmid to label up to six layer-2/3 cells in the right visual cortex of each mouse. After allowing 3–10 days for GFP expression, we imaged the axonal projections of the labelled neurons by whole-brain serial two-photon tomography with $1 \times 1 \times 10\text{-}\mu m^3$ resolution[23,24] (Fig. 1b). We then traced each fluorescently labelled cell ($n = 71$; Fig. 1c, d) and registered each brain to the Allen Reference Atlas[25] (Fig. 1e, f). To assess axonal labelling with GFP, we electroporated neurons labelled retrogradely from the ipsilateral striatum, and in all cases observed axonal terminations therein ($n = 9/9$ cells; Extended Data Fig. 1), indicating a low false-negative rate of filling axon collaterals in distal targets of V1 neurons. Nonetheless, to minimize any possible contribution of incomplete axonal filling, we excluded those reconstructed V1 neurons with axon collaterals beyond V1 that terminated abruptly without branching ($n = 28$; Extended Data Fig. 2 and Supplementary Note 1), although the results below are robust to the inclusion of these cells (Extended Data Fig. 2e). We did not exclude neurons with abrupt terminations of contralaterally projecting branches (see also ref. 6), instead restricting our analysis to ipsilaterally projecting axons.

We analysed the ipsilateral projection patterns of 38 pyramidal neurons in layer 2/3, including 31 neurons in area V1 (Fig. 1g and Extended Data Figs 3, 4) and 7 neurons in nearby higher visual areas (Extended Data Fig. 5). Inspection of individual axonal arborizations of V1

[1]Department of Neurobiology, School of Basic Medicine and Tongji Medical College, Huazhong University of Science and Technology, Wuhan, China. [2]Institute for Brain Research, Collaborative Innovation Center for Brain Science, Huazhong University of Science and Technology, Wuhan, China. [3]Biozentrum, University of Basel, 4056 Basel, Switzerland. [4]Watson School of Biological Sciences, Cold Spring Harbor, New York, USA. [5]Cold Spring Harbor Laboratory, Cold Spring Harbor, New York, USA. [6]Sainsbury Wellcome Centre, University College London, London, UK.
*These authors contributed equally to this work.
§These authors jointly supervised this work.

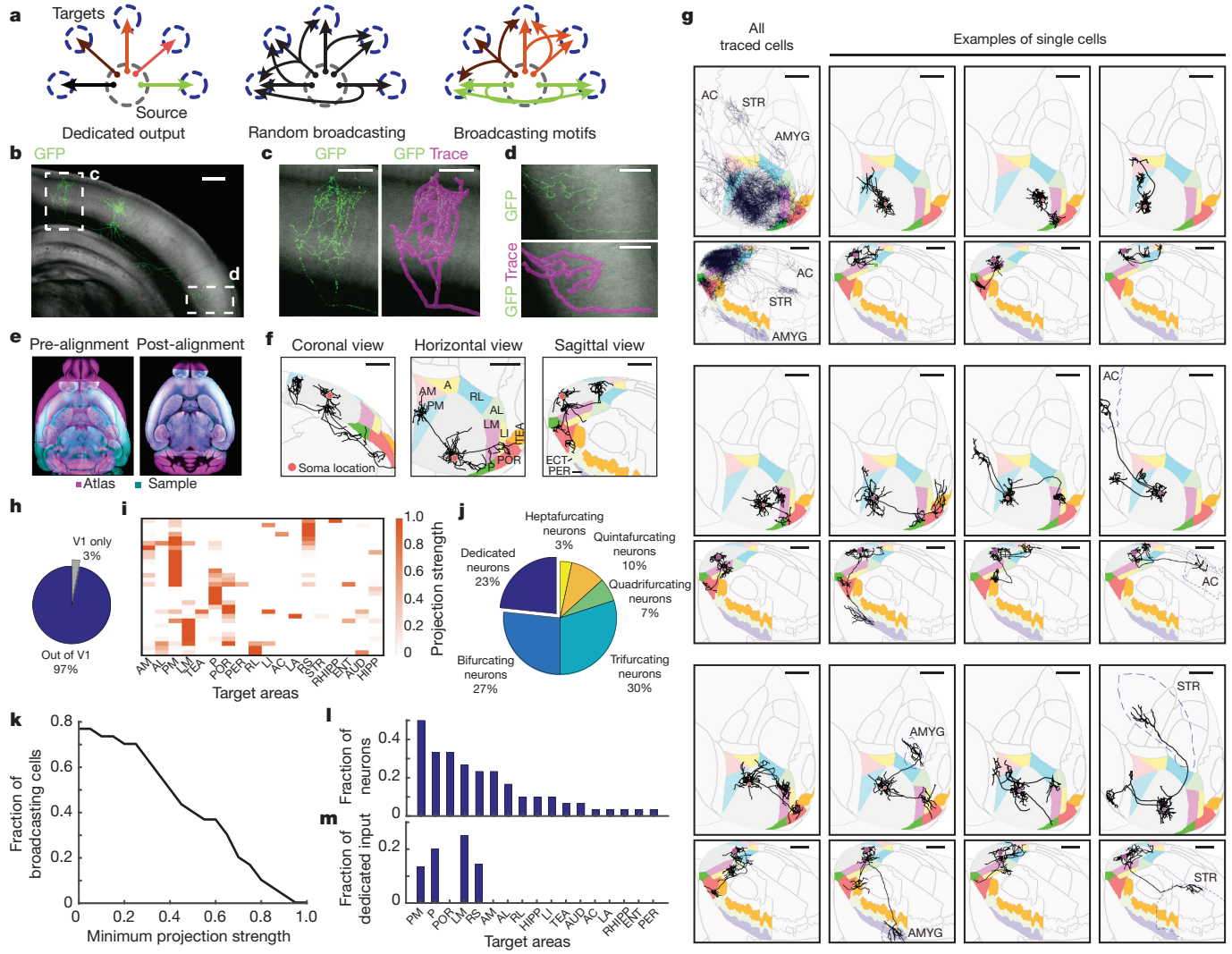

Figure 1 | Brain-wide single-cell tracing reveals the diversity of axonal projection patterns of layer-2/3 V1 neurons, with most cells projecting to more than one target area. a, Three hypothetical modes of information transfer from one source area to multiple target areas. Neurons (arrows) could each project to a single area (left) or to several areas either randomly (middle) or in predefined projection patterns (right). **b**, Maximum projection of the coronal view of a representative GFP-filled neuron acquired by serial-section two-photon microscopy. Auto-fluorescence from the red channel is used to show the brain's ultrastructure (grey background). Scale bar, 600 μm. $n = 71$ neurons. **c**, **d**, Higher magnification of the medial (**c**) and lateral (**d**) axonal arborization of the example neuron. Scale bars, 300 μm. **e**, Horizontal section through a sample brain (cyan) and the Allen Reference Atlas (purple) before (left) and after (right) rigid and non-rigid transformation of the brain to the atlas. **f**, Coronal, horizontal and sagittal projections of the traced example neuron overlaid in the Allen Reference Atlas space. Target cortical areas are coloured as indicated. A, anterior; AL, anterolateral; AM, anteromedial; ECT, ectorhinal; LI, laterointermediate; LM, lateromedial; P, posterior; PER, perirhinal; PM, posteromedial; POR, postrhinal; RL, rostrolateral; TEA, temporal association. Scale bars, 1 mm. **g**, Overlay of all traced single neurons (top left) and 11 example cells in Allen Reference Atlas space; horizontal view (top) and sagittal view (bottom) of each cell. Dashed outlines label non-visual target areas. AC, anterior cingulate cortex; AMYG, amygdala; STR, striatum. Note that these images are for illustration purposes only, because a two-dimensional projection cannot faithfully capture the true three-dimensional axonal arborization pattern. Scale bar, 1 mm. **h**, The fraction of traced single neurons that project to at least one target area outside V1 is shown in blue. At least 1 mm of axonal innervation is required for an area to be considered a target. **i**, Projection pattern of all GFP-filled V1 neurons targeted randomly ($n = 31$ neurons). The colour code reflects the projection strengths of each neuron, determined as axon length per target area, normalized to the axon length in the target area receiving the densest innervation. Only brain areas that receive input from at least one neuron, as well as the striatum, are shown. AUD, auditory cortex; ENT, entorhinal; HIPP, hippocampus; LA, lateral amygdala; RHIPP, retrohippocampal region; RS, retrosplenial. **j**, The number of projection targets for every neuron that projects out of V1. **k**, The proportion of cells targeting more than one area, when projection targets that receive projections weaker than the indicated projection strength are ignored. For each neuron, projection strengths are normalized to axon length in the target area receiving the densest innervation. **l**, The fraction of neurons projecting to each of the 18 target areas of V1. **m**, The fraction of neurons innervating a single target area ('dedicated' projection neurons) out of all neurons that innervate that area.

neurons revealed a high degree of diversity in the projections regarding the number and identity of target areas (Fig. 1g and Extended Data Figs 3, 4), whereas this diversity was not clear in the bulk projection data[20,21] (Fig. 1g, top left).

Almost all layer-2/3 cells projected out of V1 (97%, $n = 30/31$; Fig. 1h) to one or more of 18 target areas in the telencephalon (Fig. 1i), typically innervating nearby cortical areas but occasionally also projecting to the anterior cingulate cortex, striatum (Extended Data Fig. 1) and amygdala. To mitigate errors arising both from technical noise in atlas registration and from subject-to-subject variability in the boundaries between brain areas, we excluded low-confidence buffer zones of 100 μm around the area boundaries from analysis, and included only those areas that received over 1 mm of axonal input from an individual cell as targets (see Methods). Eighty-five per cent of all projection

patterns appeared only once, highlighting the diversity of long-range projections.

The majority of reconstructed layer-2/3 projection neurons sent axon collaterals to more than one target area (77%, $n = 23/30$), with some targeting up to seven areas (Fig. 1j). Although individual neurons innervated different target areas with different axonal densities, and thus might influence the computations in one area more than another, we found that a large fraction of 'broadcasting' cells innervated more than one target with comparable strengths (Fig. 1k). Moreover, the total length of axons scaled with the number of target areas (average length per brain area $= 4.6 \pm 2.2$ mm), such that the innervation density per target was, on average, similar irrespective of how many targets an axon innervated (Extended Data Fig. 6a, b). The innervation in higher visual areas was most dense in layers 2/3 and 5, consistent with recent reports[26,27], often recapitulating the pattern of lateral axonal projections of layer-2/3 cells within V1 (Extended Data Fig. 6c–h).

Posterior, postrhinal (POR), lateromedial (LM) and PM visual areas were the most common targets of V1 neurons (Fig. 1l). Even when the analysis was restricted to neurons that projected to at least one of the six nearby cortical visual areas (laterointermediate (LI), LM, AL, PM, anteromedial (AM) or rostrolateral (RL)), we found that half of these neurons projected to two or more of these areas (Extended Data Fig. 7a–e). The fraction of input provided by dedicated projection neurons to any area comprised no more than 25% of the total input (Fig. 1m), and most target areas received no dedicated input. These conclusions were robust to changes in the size of the border exclusion zone between neighbouring areas and the minimum projection strength in the target area (Extended Data Fig. 7f–h). Similar to projections from V1, all seven reconstructed neurons, which had cell bodies that resided in nearby higher visual areas, also projected to more than one target area (Extended Data Fig. 5). Our results thus show that most layer-2/3 neurons distribute information to multiple areas, rather than project to single targets.

Interestingly, the location of the cell body within V1 was predictive of projection target for some recipient areas (Extended Data Fig. 8). Given the retinotopic organization of V1, this suggests that visual information from different parts of visual field may be preferentially distributed to specific target areas, which is consistent with recent findings[28].

High-throughput MAPseq tracing

We next investigated whether broadcasting cells choose their cortical target areas independently, or whether they target specific subsets of areas. Although the targeting of different combinations of areas distinguishes individual V1 projection neurons (Fig. 1), their classification into putative sub-types requires a demonstration of higher-order projectional structure within the population. We define the higher-order structure in terms of the connection patterns predicted by the per-neuron (first-order) probability of projecting to each target. For example, if the probability of any given neuron projecting to area A is 0.5 and the probability of projecting to area B is also 0.5 then we would expect $P(A \cap B) = P(A) \times P(B) = 0.25$ of all neurons to project to both A and B if the decision to target these areas is independent. Significant deviations from this expectation would indicate the organization of the projections into non-random projection motifs. Investigating the higher-order structure requires large datasets, because, if a sample size of n neurons is required to estimate the first-order probabilities, then a sample size of n^2 is needed to estimate pairwise probabilities with comparable accuracy. Although single-neuron reconstruction provides very high spatial resolution, the tracing of axons remains highly labour intensive despite increases in throughput for data acquisition[17,29].

We therefore used a higher-throughput strategy, MAPseq[30], to obtain the required number of single-neuron projections for higher-order statistical analysis. In a MAPseq experiment, hundreds or thousands of neurons are labelled uniquely with random RNA sequences (barcodes) by a single injection of a library of barcoded Sindbis viruses (Supplementary Note 2). The barcodes are expressed and then actively transported into the axonal processes of each labelled neuron, where they can be analysed by high-throughput barcode sequencing after dissection of potential target areas. The abundance of each barcode sequence in each area serves as a measure of the projection strength of the corresponding barcode-labelled neuron. MAPseq simultaneously maps the projections of all labelled neurons of dissected target areas, and therefore enables in-depth analysis of projections to a smaller set of targets.

We used MAPseq to map the projection patterns of 553 neurons from V1 to six higher visual areas—LI, LM, AL, AM, PM and RL—that can be identified reliably by intrinsic signal imaging *in vivo* and dissected *ex vivo* for barcode sequencing (Fig. 2a, b, Extended Data Fig. 9 and Methods). To prevent the virus from spreading from V1 to adjacent areas, we made small focal injections of the MAPseq virus to yield 100–200 traced cells per mouse. Consistent with the analysis of fluorescence-based single-neuron reconstructions restricted to the six higher visual areas (Fig. 2c, left), almost half (44%) of all MAPseq neurons projected to more than one area (Fig. 2c, right). Furthermore, the projection patterns obtained by fluorescence-based tracing were statistically indistinguishable from those obtained by MAPseq (using a bootstrap procedure; see Supplementary Note 3), whereas randomly generated neurons with projection strengths sampled from a uniform distribution were markedly different (Fig. 2d). Therefore, the findings from the MAPseq dataset were consistent with those from the single-neuron tracing dataset.

We first catalogued the diversity of single-neuron projection patterns from V1 to six higher visual areas by unsupervised clustering of the MAPseq dataset (k-means clustering with a cosine distance metric). These projectional data were best described by eight clusters (Fig. 2e, Extended Data Fig. 10), of which all but one contained cells targeting more than one area. The most common combination of broadcasting neurons involved areas LM and PM, consistent with the fact that a large fraction of neurons targeted these areas and the suggestion of LM[22] and PM as integrative hubs of V1 signals, similar to the secondary visual cortex in the monkey (Fig. 2f).

To investigate whether non-random projection motifs existed in the MAPseq dataset, we measured the likelihood of specific bi-, tri- or quadrifurcations and compared them to their expected probabilities (assuming independence between each projection type; Fig. 3a, b). This analysis identified six projection motifs that were significantly over- or underrepresented after a correction for multiple comparisons (Bonferroni adjustment; Fig. 3b, c). Together, these six projection motifs represented 73% of all broadcasting cells that were identified by MAPseq. Therefore the majority of V1 cells projecting to multiple target areas do so in a non-random manner, suggesting that broadcasting motifs reflect several sub-classes of projection neurons for divergent information transfer from V1 to higher visual areas.

The most underrepresented broadcasting motif was the bifurcation between PM and AL (Fig. 3d). These two areas exhibit distinct visual response properties[13,14] and receive functionally specialized input from V1[7], consistent with the idea of exclusive projections from V1 into these areas. Moreover, the underrepresented population of neurons, which project to both PM and AL, was further split into two groups according to projection strength; one population primarily innervates PM and another primarily innervates AL (Fig. 3d). A second underrepresented motif is the bifurcation between PM and LM (Fig. 3e). However, in contrast to the PM–AL bifurcation, the detected PM–LM-projection neurons do not clearly separate into two classes. Our findings therefore provide an anatomical substrate for the previously reported functional dichotomy of AL and PM areas, and suggest that a few 'dedicated' output channels can co-exist with the prevalence of broadcasting cells that co-innervate multiple targets.

In addition to the two underrepresented projectional motifs, we identified four overrepresented motifs, that is, combinations of target areas that receive more shared input from individual V1 neurons than expected from first-order projection statistics (Fig. 3f–h). Cells

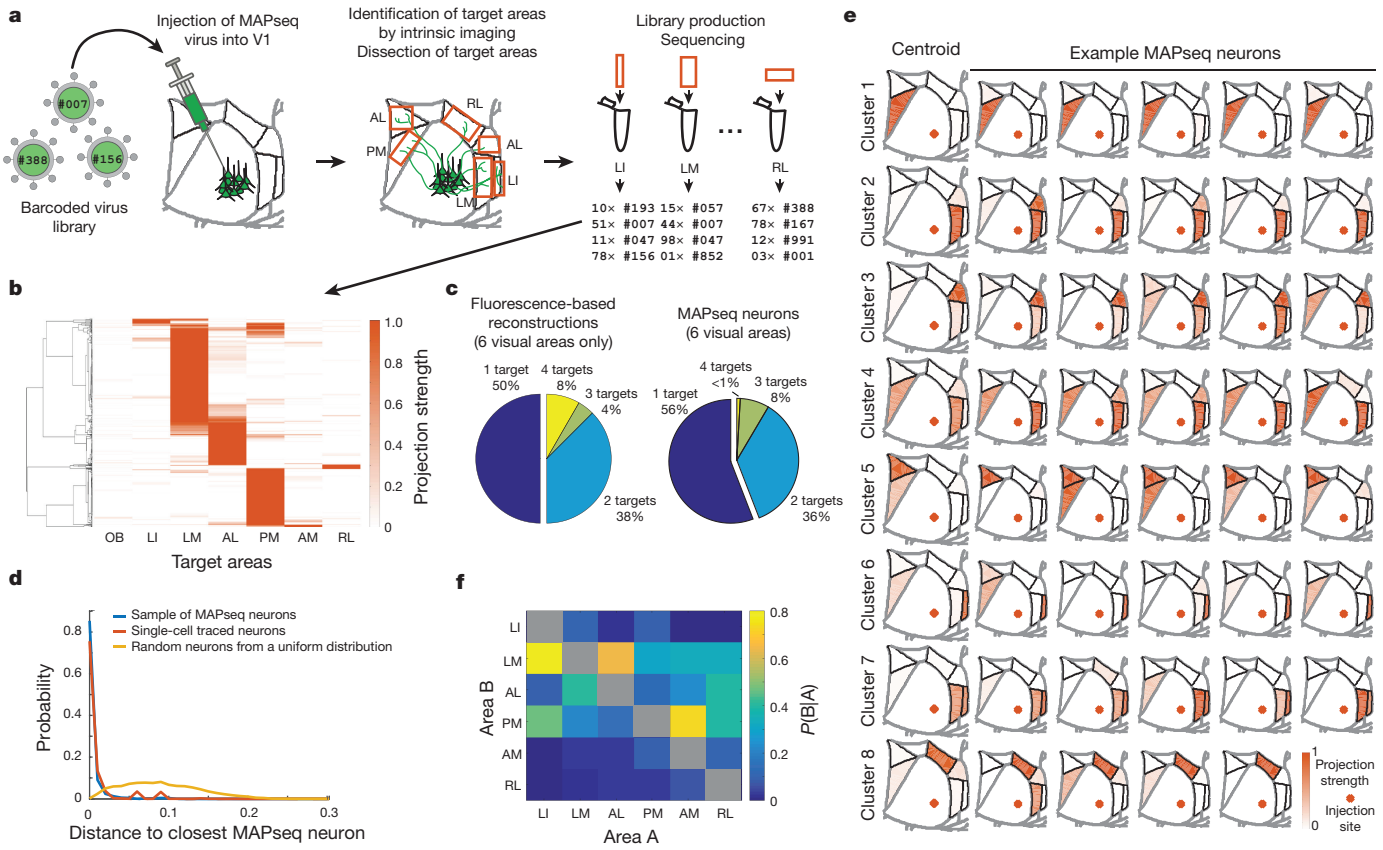

Figure 2 | MAPseq projection mapping reveals a diversity of projection motifs. a, Overview of the MAPseq procedure. Six target areas were chosen for analysis: LI, LM, AL, PM, AM and RL. **b**, Projection strength in the six target areas, as well as the olfactory bulb (OB) as a negative control, of 553 neurons mapped using MAPseq. Projection strengths per neuron are defined as the number of barcode copies per area, normalized to the efficiency of sequencing library generation and to the neuron's maximum projection strength ($n = 4$ mice). **c**, Number of projection targets of V1 neurons when considering the six target areas only, based on the fluorescence-based axonal reconstructions (left) or the MAPseq data (right). **d**, Distribution of cosine distances obtained by a bootstrapping procedure (1,000 repeats) between MAPseq neurons (blue), fluorescence-based single-neuron reconstructions and MAPseq neurons (orange), or random neurons (with projection strengths sampled from a uniform distribution) and MAPseq neurons (yellow). The distance distributions obtained from MAPseq neurons and fluorescence-based single-neuron reconstructions are statistically indistinguishable (Kolmogorov–Smirnov one-sided two-sample test; $P = 0.94$; $\alpha = 0.05$), whereas the distributions obtained from both MAPseq neurons or fluorescence-based reconstructed neurons are statistically different from the distribution obtained using random neurons (Kolmogorov–Smirnov two-sample test; $P < 10^{-3}$; $\alpha = 0.05$). **e**, Centroids and example cells for eight clusters obtained by *k*-means clustering of all MAPseq cells using a cosine distance metric. Target areas are coloured to indicate the projection strength of the plotted neuron. Projection strengths are normalized as in **b**. **f**, The probability of projecting to one area (area A) given that the same neuron is projecting to another area (area B) based on the MAPseq dataset.

that innervated both PM and AM were significantly more abundant than expected by chance (Fig. 3f). Resolving the projection strengths within this motif revealed two subpopulations of neurons, one that innervates PM more than AM, the other innervates both areas with similar strength. Moreover, neurons bifurcating to LM and AL were also highly overrepresented (Fig. 3g) and comprised the most abundant class of broadcasting cells (Fig. 3b). The most significantly overrepresented trifurcation motif was the projection to PM, LM and LI, comprising a relatively homogenous population that projects to LM and PM with similar strengths while projecting slightly less strongly to LI (Fig. 3h). Finally, we discovered that trifurcation between PM, AM and RL was overrepresented, but it appeared only rarely in our dataset (Fig. 3b). These motifs did not arise from false negatives (undetected connections) or false positives (Supplementary Note 4 and Extended Data Fig. 2f).

These projectional data have implications for the categorization of higher visual areas into putative streams of visual processing in mouse neocortex. Areas AL and PM on the one hand, and LM and LI on the other, have been suggested to belong to dorsal and ventral processing streams in the mouse visual system, respectively[31–33]. Given that these areas receive a high degree of shared input (for example, LM–PM bifurcation, which was still abundant even though it was underrepresented; AL–LM bifurcation; PM–LM–LI trifurcation), such a distinction is unlikely to originate as a result of segregated V1 input into these areas.

Discussion

In summary, our results reveal some of the principles by which single neurons in one cortical area distribute information to downstream target areas. Almost all layer-2/3 pyramidal cells projected outside of V1, indicating that V1 neurons concurrently participate in local and distal computations. We found that the single-neuron projections outside V1 were highly diverse, innervating up to seven targets, predominantly in specific, non-random combinations (Extended Data Fig. 10g, f). These results suggest a functional specialization of subpopulations of projection cells beyond 'one neuron–one target area' mapping.

The fraction of neurons in V1 that broadcast information to multiple targets is considerably greater than has previously been indicated using retrograde tracing methods[2,5,16]. This difference is unlikely to be caused by differences in the sensitivity with which these approaches detect the projection patterns of individual cells. Instead, anterograde tracing maps projections to many or all targets simultaneously, whereas

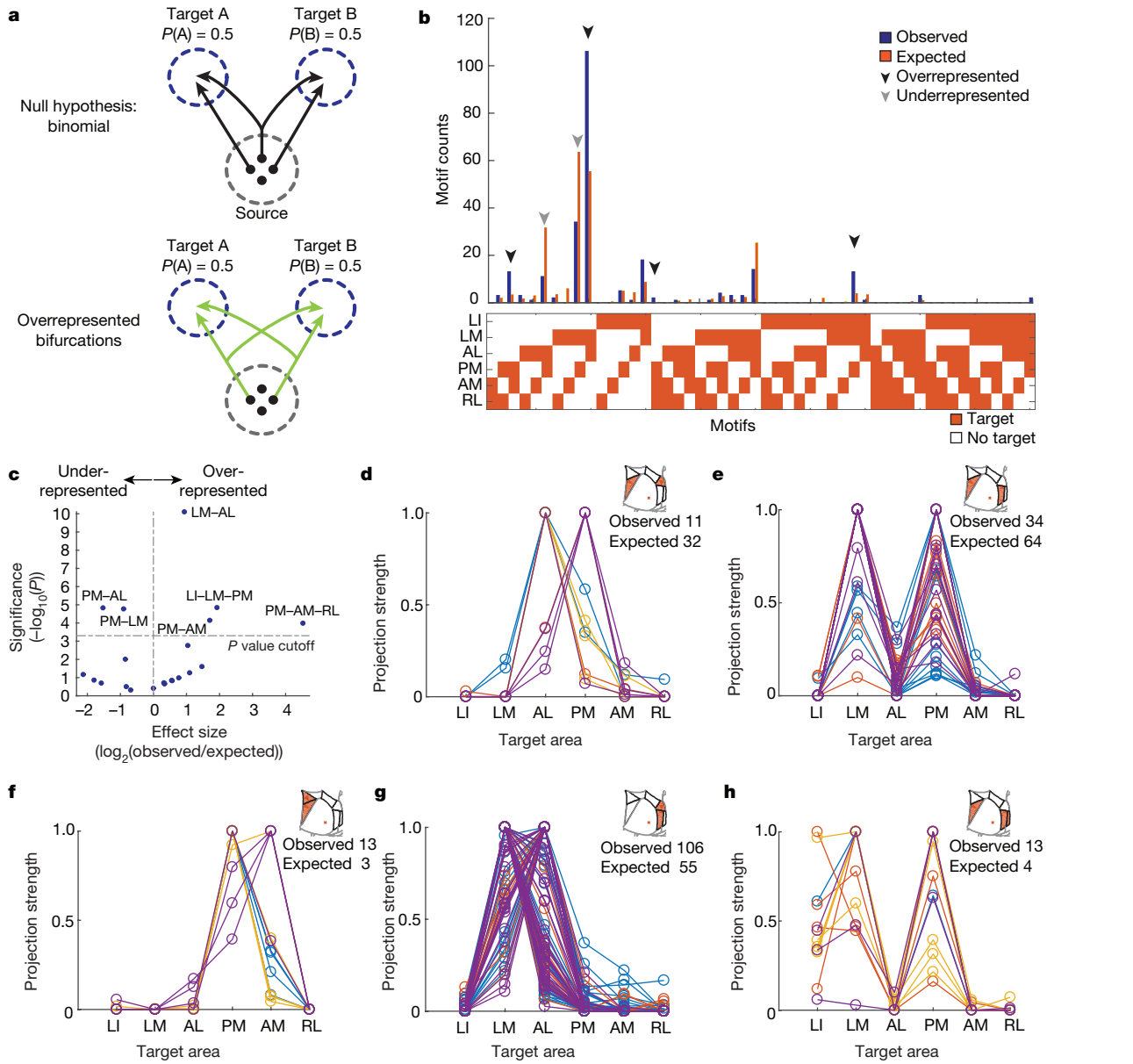

Figure 3 | Over- and underrepresented projection motifs of neurons in V1. a, The null hypothesis of independent projections to two target areas (top) and an example deviation (overrepresented bifurcation) from the null hypothesis (bottom). **b**, The observed and expected abundance of all possible bi-, tri- and quadrifurcation motifs in the MAPseq dataset. Significantly over- or underrepresented motifs, based on a binomial test with Bonferroni correction (see Methods), are indicated by black and grey arrowheads, respectively. $n = 553$ neurons from four mice. **c**, Statistical significance of over- and underrepresented broadcasting motifs and associated effect sizes, based on a binomial test with Bonferroni correction (see Methods). $n = 553$ neurons from four mice. **d**–**h**, The projection strengths of the individual neurons (one per line) giving rise to the six underrepresented (**d**, **e**) and overrepresented (**f**–**h**) projection motifs. For each neuron, the projection strength in each target area is normalized to the neuron's maximum projection strength. Lines of the same colour represent neurons mapped in the same brain ($n = 4$ mice).

retrograde tracing typically analyses only two or three potential target sites at a time. Because the fraction of neurons projecting to any pair of targets selected for retrograde tracing is relatively low (typically $<10\%$), most neurons will not be doubly labelled in any given experiment; only by sampling many potential targets in a single experiment can the true prevalence of broadcasting be uncovered. Indeed, if we simulate double retrograde tracing based on our MAPseq results, the fractions of bifurcating neurons are comparable to those observed when using retrograde methods in primates[2,5,16,18] (Supplementary Table 1).

We speculate that dedicated projection neurons—which comprise the minority of neurons in V1—convey specialized visual information that is tailored to their target area, as has previously been suggested[6–11]. Indeed, the most underrepresented projection motif from V1, the PM–AL bifurcation, innervates two target areas with distinct preferences for visual features[13,14]. By contrast, we suggest that the majority of cells encode information that is shared and in a form that is suitable for generating visual representations or multimodal associations across subsets of areas. Indeed, those target areas that are preferentially co-innervated by broadcasting neurons appear to have more similar visual response properties[13,14]. Broadcasting cells may also coordinate activity among the subset of areas that they co-innervate, thus providing a signal that links different processing streams. The divergent nature of signal transmission from a primary sensory cortex to its targets may therefore help to constrain models of hierarchical sensory processing. The existence of distinct projection motifs that either avoid or favour subsets of target areas suggests that sub-types of intracortical projection neurons exist and raises the question of how these specific, long-range connectivity patterns are established during development.

Online Content Methods, along with any additional Extended Data display items and Source Data, are available in the online version of the paper; references unique to these sections appear only in the online paper.

Received 14 June 2017; accepted 31 January 2018.
Published online 28 March 2018.

1. Harris, K. D. & Shepherd, G. M. G. The neocortical circuit: themes and variations. *Nat. Neurosci.* **18,** 170–181 (2015).
2. Nakamura, H., Gattass, R., Desimone, R. & Ungerleider, L. G. The modular organization of projections from areas V1 and V2 to areas V4 and TEO in macaques. *J. Neurosci.* **13,** 3681–3691 (1993).
3. Segraves, M. A. & Innocenti, G. M. Comparison of the distributions of ipsilaterally and contralaterally projecting corticocortical neurons in cat visual cortex using two fluorescent tracers. *J. Neurosci.* **5,** 2107–2118 (1985).
4. Rockland, K. S. Collateral branching of long-distance cortical projections in monkey. *J. Comp. Neurol.* **521,** 4112–4123 (2013).
5. Sincich, L. C. & Horton, J. C. Independent projection streams from macaque striate cortex to the second visual area and middle temporal area. *J. Neurosci.* **23,** 5684–5692 (2003).
6. Yamashita, T. *et al.* Membrane potential dynamics of neocortical projection neurons driving target-specific signals. *Neuron* **80,** 1477–1490 (2013).
7. Glickfeld, L. L., Andermann, M. L., Bonin, V. & Reid, R. C. Cortico-cortical projections in mouse visual cortex are functionally target specific. *Nat. Neurosci.* **16,** 219–226 (2013).
8. Sato, T. R. & Svoboda, K. The functional properties of barrel cortex neurons projecting to the primary motor cortex. *J. Neurosci.* **30,** 4256–4260 (2010).
9. Chen, J. L., Carta, S., Soldado-Magraner, J., Schneider, B. L. & Helmchen, F. Behaviour-dependent recruitment of long-range projection neurons in somatosensory cortex. *Nature* **499,** 336–340 (2013).
10. Yamashita, T. & Petersen, C. C. H. Target-specific membrane potential dynamics of neocortical projection neurons during goal-directed behavior. *eLife* **5,** e15798 (2016).
11. Movshon, J. A. & Newsome, W. T. Visual response properties of striate cortical neurons projecting to area MT in macaque monkeys. *J. Neurosci.* **16,** 7733–7741 (1996).
12. Nassi, J. J. & Callaway, E. M. Parallel processing strategies of the primate visual system. *Nat. Rev. Neurosci.* **10,** 360–372 (2009).
13. Andermann, M. L., Kerlin, A. M., Roumis, D. K., Glickfeld, L. L. & Reid, R. C. Functional specialization of mouse higher visual cortical areas. *Neuron* **72,** 1025–1039 (2011).
14. Marshel, J. H. H., Garrett, M. E. E., Nauhaus, I. & Callaway, E. M. M. Functional specialization of seven mouse visual cortical areas. *Neuron* **72,** 1040–1054 (2011). 8
15. Massé, I. O., Régnier, P & Boire, D. in *Axons and Brain Architecture* (ed. Rockland, K. S.) Ch. 5, 93–116 (Academic, 2016).
16. Bullier, J. & Kennedy, H. Axonal bifurcation in the visual system. *Trends Neurosci.* **10,** 205–210 (1987).
17. Economo, M. N. *et al.* A platform for brain-wide imaging and reconstruction of individual neurons. *eLife* **5,** e10566 (2016).
18. Vogt Weisenhorn, D. M., Illing, R. B. & Spatz, W. B. Morphology and connections of neurons in area 17 projecting to the extrastriate areas MT and 19DM and to the superior colliculus in the monkey *Callithrix jacchus*. *J. Comp. Neurol.* **362,** 233–255 (1995).
19. Ding, S.-L., Van Hoesen, G. & Rockland, K. S. Inferior parietal lobule projections to the presubiculum and neighboring ventromedial temporal cortical areas. *J. Comp. Neurol.* **425,** 510–530 (2000).
20. Zingg, B. *et al.* Neural networks of the mouse neocortex. *Cell* **156,** 1096–1111 (2014).
21. Oh, S. W. *et al.* A mesoscale connectome of the mouse brain. *Nature* **508,** 207–214 (2014).
22. Wang, Q. & Burkhalter, A. Area map of mouse visual cortex. *J. Comp. Neurol.* **502,** 339–357 (2007).
23. Ragan, T. *et al.* Serial two-photon tomography for automated *ex vivo* mouse brain imaging. *Nat. Methods* **9,** 255–258 (2012).
24. Osten, P. & Margrie, T. W. Mapping brain circuitry with a light microscope. *Nat. Methods* **10,** 515–523 (2013).
25. Lein, E. S. *et al.* Genome-wide atlas of gene expression in the adult mouse brain. *Nature* **445,** 168–176 (2007).
26. D'Souza, R. D., Meier, A. M., Bista, P., Wang, Q. & Burkhalter, A. Recruitment of inhibition and excitation across mouse visual cortex depends on the hierarchy of interconnecting areas. *eLife* **5,** e19332 (2016).
27. Yang, W., Carrasquillo, Y., Hooks, B. M., Nerbonne, J. M. & Burkhalter, A. Distinct balance of excitation and inhibition in an interareal feedforward and feedback circuit of mouse visual cortex. *J. Neurosci.* **33,** 17373–17384 (2013).
28. Zhuang, J. *et al.* An extended retinotopic map of mouse cortex. *eLife* **6,** e18372 (2017).
29. Gong, H. *et al.* High-throughput dual-colour precision imaging for brain-wide connectome with cytoarchitectonic landmarks at the cellular level. *Nat. Commun.* **7,** 12142 (2016).
30. Kebschull, J. M. *et al.* High-throughput mapping of single-neuron projections by sequencing of barcoded RNA. *Neuron* **91,** 975–987 (2016).
31. Wang, Q., Sporns, O. & Burkhalter, A. Network analysis of corticocortical connections reveals ventral and dorsal processing streams in mouse visual cortex. *J. Neurosci.* **32,** 4386–4399 (2012).
32. Smith, I. T., Townsend, L. B., Huh, R., Zhu, H. & Smith, S. L. Stream-dependent development of higher visual cortical areas. *Nat. Neurosci.* **20,** 200–208 (2017).
33. Murakami, T., Matsui, T. & Ohki, K. Functional segregation and development of mouse higher visual areas. *J. Neurosci.* **37,** 9424–9437 (2017).

Supplementary Information is available in the online version of the paper.

Acknowledgements We thank A. Juavinett, L. Huang, S. Hofer and P. Znamenskiy for comments on the manuscript. This study was funded by National Institutes of Health (5RO1NS073129 and 5RO1DA036913 to A.M.Z.); Brain Research Foundation (BRF-SIA-2014-03 to A.M.Z.); IARPA (MICrONS D16PC0008 to A.M.Z.); Simons Foundation (382793/SIMONS to A.M.Z.); Paul Allen Distinguished Investigator Award (to A.M.Z.); PhD fellowship from the Boehringer Ingelheim Fonds (to J.M.K.); PhD fellowship from the Genentech Foundation (to J.M.K.); National Natural Science Foundation of China (NSFC 31600847 to Y.H.); European Research Council (NeuroV1sion 616509 to T.D.M.-F.), and Swiss National Science Foundation (SNSF 31003A_169802 to T.D.M.-F.).

Author Contributions Y.H. generated the dataset for fluorescence-based axonal tracing. D.C. and Y.H. traced the cells. R.A.A.C. analysed the serial two-photon imaging data and axonal projection patterns. J.M.K. and F.I. collected the MAPseq dataset. J.M.K. and A.M.Z. performed the analysis of projection patterns. J.M.K., T.D.M.-F. and A.M.Z. wrote the paper.

Author Information Reprints and permissions information is available at www.nature.com/reprints. The authors declare no competing financial interests. Readers are welcome to comment on the online version of the paper. Publisher's note: Springer Nature remains neutral with regard to jurisdictional claims in published maps and institutional affiliations. Correspondence and requests for materials should be addressed to A.M.Z. (zador@cshl.edu) or T.D.M.-F. (t.mrsic-flogel@ucl.ac.uk).

Reviewer Information *Nature* thanks M. Helmstaedter, O. Sporns and the other anonymous reviewer(s) for their contribution to the peer review of this work.

METHODS

Mice. The anatomical single-cell tracing experiments were conducted at The Biozentrum, University of Basel, Switzerland. We obtained licenses and performed all experimental procedures in accordance with Basel Canton animal welfare guidelines using both male and female adult (>8 weeks of age) C57BL/6 mice. Detailed protocols and all software are available at http://mouse.vision/han2017.

Fluorescence-based single-neuron tracing. *Two-photon guided single-cell electroporation.* We performed surgery as previously described[34]. In brief, we anaesthetized mice with a mixture of fentanyl (0.05 mg kg^{-1}), midazolam (5 mg kg^{-1}) and medetomidine (0.5 mg kg^{-1}), and maintained stable anaesthesia by isoflurane (0.5% in O_2). We performed all electroporation experiments on a custom linear scanning two-photon microscope, equipped to image both a green and a red channel and running ScanImage 5.1[35]. For electroporation, we used a patch pipette (12–16 MΩ) filled with plasmid DNA (pCAG-eGFP (Addgene, 11150) or pAAV-EF1a-eGFP-WPRE (gift from B. Roska; sequence file can be found in the Supplementary Information, 100 ng μl^{-1}) and AlexaFluor 488 (50 μM) in intracellular solution, and delivered electroporation pulses (100 Hz, −14 V, 0.5-ms duration for 1 s) with an Axoporator 800A (Molecular Probes) when pushed against a target cell. We verified successful electroporation by dye filling of the cell body, and then sealed the skull with a chronic window using 1.5% agarose in HEPES-buffered artificial cerebrospinal fluid and a cover slip. We confirmed plasmid expression two days after electroporation by visualization of GFP epifluorescence through the chronic imaging window. Three to ten days after electroporation, we transcardially perfused anaesthetized mice with 10 ml 0.9% NaCl followed by 50 ml 4% paraformaldehyde in 0.1 M phosphate buffer (pH 7.4). We removed the brains from the skull and post-fixed them in 4% paraformaldehyde overnight at 4 °C. We then stored the fixed brains in PBS at 4 °C until imaging with serial-section two-photon tomography.

Serial-section two-photon tomography. We embedded the fixed brains in 5% oxidized agarose (derived from type-I agarose (Sigma-Aldrich)) and covalently cross-linked the brain to the agarose by incubation in an excess of 0.5–1% sodium borohydride ($NaBH_4$, Sigma-Aldrich) in 0.05 M sodium borate buffer overnight at 4 °C. We then imaged embedded brains using a TissueVision two-photon scanning microscope[23,36], which cut physical sections of the entire brain every 50 μm coronally, and acquired optical sections every 10 μm in two channels (green channel: 500–560 nm; red channel: 560-650 nm) using 940-nm excitation laser light (Mai Tai eHP, Spectraphysics). Each imaged section is formed from overlapping 800 × 800-μm 'tiles'. We imaged with a resolution of 1 μm in *x* and *y* and measured an axial point spread function of ∼5 μm FWHM (full width at half maximum) using ScanImage 5.1.

Image processing and cell tracing. We stitched raw image tiles using custom MATLAB-based software, StitchIt. StitchIt applies illumination correction based on the average tiles for each channel and optical plane, and subsequently stitches the illumination-corrected tiles from the entire brain. We then navigated through the stitched brain space using MaSIV (https://github.com/alexanderbrown/masiv), a MATLAB-based viewer for very large 3D images, and traced axons using a custom, manual neurite-tracing extension for MaSIV. The tracer was not blinded, as no comparison across experimental conditions was performed. No power calculations were performed.

To assign each voxel of the imaged brains to a brain area, we segmented each brain using areas defined by the Allen Reference Atlas (Common Coordinate Framework v.3, © 2015 Allen Institute for Brain Science, Allen Brain Atlas API, available from http://brain-map.org/api/index.html), after smoothing with a single pass of a Gaussian kernel with an s.d. of 0.5 using the Nifty 'seg-maths' tool as described previously[37]. In brief, we downsampled one imaging channel to a voxel size of 25 μm and converted it to MHD format using StitchIt. We then registered the volume to the average template brain of the Allen Reference Atlas using Elastix[38] by applying rigid affine transformation followed by non-rigid deformation with parameters as previously described[39,40]. We examined registration quality using a custom Python/PyQt5 application, Lasagna, which overlays the Allen template brain and the registered sample brain and is extendable to allow the overlay of traced cells, or the overlay of area borders from the Allen Reference Atlas onto a downsampled brain. To transform the traced cells into Allen Reference Atlas space (sample to the Allen Reference Atlas), we calculated the inverse transform to the one calculated by Elastix (Allen Reference Atlas to sample) and applied this to the traced points.

Analysis of traced neurons. To prevent potential incomplete filling of neurons from biasing the results of our analyses, we excluded cells with non-arborizing primary branches in the ipsilateral hemisphere from the analysis. Out of a total of 71 traced cells, we excluded 28 cells that exhibited abrupt, non-callosal terminations, as well as 5 cells that were back-labelled from the striatum, thus restricting our analysis to ipsilateral projection patterns of 31 cells in V1 and 7 in other higher visual areas. Moreover, axonal branches terminating contralaterally or after entering the corpus callosum were considered as callosal terminations and were included in the analysis (see also ref. 6). We calculated the first-order projection statistics only using the cells registered in the Allen Reference Atlas that satisfied these criteria. To reduce any artefacts associated with registration in the Allen Reference Atlas or individual brain variability in boundaries between brain areas, we excluded any axon within 50 μm from any brain area boundary from the analysis. We then calculated the projection strength of each neuron to each area as the total length of axon of that neuron in an area. To determine the number of projection targets for every cell, we used a minimum projection strength of 1-mm axon length per target area.

MAPseq. *MAPseq sample processing.* To define the V1 injection site and target higher visual areas (LI, LM, AL, PM, AM and RL), we used optical imaging of intrinsic signals as previously described[13,41]. In brief, we first implanted a customized head plate and then thinned the skull to increase its transparency. After 2–3 days of recovery, we sedated the mice (chlorprothixene, 0.7 mg kg^{-1}) and lightly anaesthetized them with isoflurane (0.5–1.5% in O_2), delivered via a nose cone. We illuminated the visual cortex with 700-nm light that was split from an LED source into two light guides, performing imaging with a tandem lens macroscope focused 250–500 μm below the cortical surface and a bandpass filter centred at 700 nm with 10-nm bandwidth (67905; Edmund Optics). We acquired images at 6.25 Hz with a 12-bit CCD camera (1300QF; VDS Vosskühler), frame grabber (PCI-1422; National Instruments) and custom software written in LabVIEW (National Instruments). We visually stimulated the contralateral eye of mice with a monitor placed at a distance of 21 cm and presented 25–35° patches of 100% contrast square wave gratings with a temporal frequency of 4 Hz and a spatial frequency of 0.02 cycles per degree for 2 s followed by 5 s of grey screen (mean luminance of 46 candela per m^2). To establish a coarse retinotopy of the targeted area, we alternated the position of the patches: we used two different elevations (approximately 0 and 20°) and two different azimuths (approximately 60 and 90°); at each position, we acquired at least 17 trials. We obtained intrinsic signal maps by averaging the responses during the stimulation time using ImageJ (National Institute of Mental Health, NIH) and mapping the location of the estimated spots of activation onto a previously acquired blood vessel picture.

We then pressure-injected (Picospritzer III, Parker) 100 nl of 1×10^{10} genome copies ml^{-1} barcoded MAPseq Sindbis virus[30] with a diversity of $>8 \times 10^6$ different barcode sequences unilaterally at a depth of 100–200 μm from the brain surface into V1 of four 8–10-week-old C57BL/6 female mice. In addition, we labelled the six higher visual areas by placing a DiI-coated micropipette into retinotopically matched positions according to intrinsic signal maps. For this, we allowed 2–5 μl of 2.5 mg ml^{-1} DiI (Invitrogen D3911) in ethanol solution to dry on the outside of a pulled micropipette tip until some DiI crystals were visible. Mice were euthanized 44–48 h after injection by decapitation, and their brain immediately extracted and flash-frozen on dry ice.

We cut 180-μm thick coronal sections using a cryostat at −10 °C blade and sample holder temperature, and melted each slice onto a clean microscope slide before rapidly freezing it on dry ice again. We then dissected each target area and the injection site using cold scalpels while keeping the brain sections frozen on a metal block cooled to approximately −20 °C in a freezing 2.25 M $CaCl_2$ bath[42]. During dissection, we identified each dissected area using a fluorescent dissection microscope to visualize viral GFP expression and DiI stabs labelling each target area (Extended Data Fig. 7). Throughout the procedure, we took care to avoid sample cross-contamination by never reusing tools or blades applied to different areas and changing gloves between samples. To measure noise introduced by contamination, we collected samples of the olfactory bulb from each brain, which served as a negative control.

We then processed the dissected samples for sequencing mostly as previously described[30], but pooling all samples after first-strand cDNA synthesis. In brief, we extracted total RNA from each sample using TRIzol reagent (Thermo Fisher) according to the manufacturer's instructions. We mixed the sample RNA with spike-in RNA (obtained by *in vitro* transcription of a double-stranded ultramer with sequence 5′-GTCATGATCATAATACGACTCACTATAG GGGACGAGCTGTACAAGTAAACGCGTAATGATACGGCGACCACCGAGA TCTACACTCTTTCCCTACACGACGCTCTTCCGATCTNNNNNNNNNNNN NNNNNNNNNNNNATCAGTCATCGGAGCGGCCGCTACCTAATTGCCG TCGTGAGGTACGACCACCGCTAGCTGTACA-3′ (IDT)[30]) and reverse transcribed the RNA mixture using a gene specific primer 5′-CTTGGCACCCGA GAATTCCANNNNNNNNNNNNXXXXXXXXTGTACAGCTAGCGGTGGT CG-3′, where X_8 is one of >300 true-seq-like sample-specific identifiers and N_{12} is the unique molecular identifier, and SuperscriptIV Reverse Transcriptase (Thermo Fisher) according to the manufacturer's instructions. We then pooled all first-strand cDNAs, purified them using SPRI beads (Beckman

Coulter) and produced double-stranded cDNA as previously described[43]. We then treated the samples using ExonucleaseI (NEB) and performed two rounds of nested PCR using primers 5′-CTCGGCATGGACGAGCTGTA-3′ and 5′-CAAGCAGAAGACGGCATACGAGATCGTGATGTGACTGGAG TTCCTTGGCACCCGAGAATTCCA-3′ for the first PCR and primers 5′-AATGATACGGCGACCACCGA-3′ and 5′-CAAGCAGAAGACGGCA TACGA-3′ for the second PCR using Accuprime Pfx polymerase (Thermo Fisher). Finally, we gel-extracted the resulting PCR amplicons using Qiagen MinElute Gel extraction kit according to the manufacturer's instructions and sequenced the library on a Illumina NextSeq500 high-output run at paired-end 36 using the SBS3T sequencing primer for paired-end 1 and the Illumina small RNA sequencing primer 2 for paired-end 2.

MAPseq data analysis. On the basis of the sequencing results, we constructed a barcode matrix M of size of (number of barcodes) × (number of dissected areas) with entry $M_{i,j}$ representing the absolute counts of barcode i in area j as previously described[30]. We de-multiplexed the sequencing results, extracted the absolute counts of each barcode in each sample based on the UMI sequence and error-corrected the barcode sequences, before matching barcode sequences to the virus library and constructing matrix M by matching barcode sequences across areas. We then filtered the barcode matrix for 'high-confidence' cell bodies inside the dissected area of V1 by requiring a minimum of 10 counts in at least one target area, an at least tenfold difference between the cell body location in V1 and the most abundant target area in data normalized to the efficiency of library production as measured by the amount of recovered spike-in RNA counts, and an absolute minimum barcode count of 300 in V1. We then normalized the raw barcode counts in each area to the relative spike-in RNA recovery to the olfactory bulb sample, merged the results from all four processed brains into a single barcode matrix and used this matrix for all further analysis.

To determine whether a particular neuron projected to any given target area, we chose a conservative threshold of at least 5 barcode counts, based on the highest level of barcode expression in the olfactory bulb negative control sample.

Calculation of statistical significance of projection motifs. To calculate the statistical significance of broadcasting projection motifs, we compared against the simplest model in which we assumed that each neuron projected to each area independently. To generate predictions of this model, we first estimated the probability of projecting to each area, assuming independent projections. We define the probability $P(A_i)$ that a given neuron projects to the ith area A_i as

$$P(A_i) = \frac{N_{A_i}}{N_{\text{total}}}$$

in which N_{A_i} is the number of neurons in the sample that project to area A_i, $\mathrm{i} = 1 \ldots k$ for k analysed target areas, and N_{total} is the total number of neurons in the sample.

In our MAPseq experiments, we do not have direct access to N_{total}, since for technical reasons we only include neurons that have at least one projection among the dissected targets. Because, in principle, some neurons might project to none of the areas dissected (see Fig. 3a), failure to include these would lead to an underestimation of N_{total}. However, assuming independence of projections, we can infer N_{total} from the available measurements.

To estimate N_{total}, we first observe that

$$P(\text{project to at least one area}) + P(\text{project to no area}) = 1$$
$$\Leftrightarrow \frac{N_{\text{obs}}}{N_{\text{total}}} + \prod_{j=1}^{k}\left(1 - \frac{N_{A_j}}{N_{\text{total}}}\right) = 1$$

where N_{obs} is the total number of neurons observed to project to at least one area. For $k = 6$ areas, we can expand this expression to

$$\left(N_{\text{obs}} - \sum_{j=1}^{6} N_{A_j}\right) N_{\text{total}}^5 + \sum_{i=1}^{6}\sum_{\substack{j=1 \\ j\neq i}}^{6} N_{A_i} N_{A_j} N_{\text{total}}^4$$
$$- \sum_{i=1}^{6}\sum_{\substack{j=1 \\ j\neq i}}^{6}\sum_{\substack{k=1 \\ k\neq j}}^{6} N_{A_i} N_{A_j} N_{A_k} N_{\text{total}}^3$$
$$+ \sum_{i=1}^{6}\sum_{\substack{j=1 \\ j\neq i}}^{6}\sum_{\substack{k=1 \\ k\neq j}}^{6}\sum_{\substack{l=1 \\ l\neq k}}^{6} N_{A_i} N_{A_j} N_{A_k} N_{A_l} N_{\text{total}}^2$$
$$- \sum_{i=1}^{6}\sum_{\substack{j=1 \\ j\neq i}}^{6}\sum_{\substack{k=1 \\ k\neq j}}^{6}\sum_{\substack{l=1 \\ l\neq k}}^{6}\sum_{\substack{m=1 \\ m\neq l}}^{6} N_{A_i} N_{A_j} N_{A_k} N_{A_l} N_{A_m} N_{\text{total}} + \prod_{i=1}^{6} N_{A_i} = 0$$

Noting that this is a quintic equation in N_{total}, we can use a root finder to solve for N_{total} numerically, and use the result to calculate $P(A_i)$.

Using the derived N_{total} and $P(A_i)$, we can calculate the P value for every possible broadcasting motif by calculating the value of the binomial cumulative distribution function, for a total of N_{total} tries, the empirical number of observed counts (successes), and P(motif) assuming independent projections. We calculated the P value of all possible bi-, tri- and quadrifurcations, and determined significantly over- or underrepresented broadcasting motifs at a significance threshold of $\alpha = 0.05$ after Bonferroni correction.

Code availability. All software is available at http://mouse.vision/han2017.

Data availability. All sequencing data are publicly available in the Sequence Read Archive under accession numbers SRR5274845 (ZL097 for mouse 4 and mouse 5) and SRR5274844 (ZL102 for mouse 6 and mouse 7). All single-cell tracing results are accessible at http://mouse.vision/han2017 and on neuromorpho at http://neuromorpho.org/NeuroMorpho_ArchiveLinkout.jsp?ARCHIVE=Han_etal.

34. Pecka, M., Han, Y., Sader, E. & Mrsic-Flogel, T. D. Experience-dependent specialization of receptive field surround for selective coding of natural scenes. *Neuron* **84,** 457–469 (2014).
35. Pologruto, T. A., Sabatini, B. L. & Svoboda, K. ScanImage: flexible software for operating laser scanning microscopes. *Biomed. Eng. Online* **2,** 13 (2003).
36. Mayerich, D., Abbott, L. & McCormick, B. Knife-edge scanning microscopy for imaging and reconstruction of three-dimensional anatomical structures of the mouse brain. *J. Microsc.* **231,** 134–143 (2008).
37. Niedworok, C. J. *et al.* aMAP is a validated pipeline for registration and segmentation of high-resolution mouse brain data. *Nat. Commun.* **7,** 11879 (2016).
38. Klein, S., Staring, M., Murphy, K., Viergever, M. A. & Pluim, J. P. elastix: a toolbox for intensity-based medical image registration. *IEEE Trans. Med. Imaging* **29,** 196–205 (2010).
39. Kim, Y. *et al.* Whole-brain mapping of neuronal activity in the learned helplessness model of depression. *Front. Neural Circuits* **10,** 3 (2016).
40. Renier, N. *et al.* Mapping of brain activity by automated volume analysis of immediate early genes. *Cell* **165,** 1789–1802 (2016).
41. Roth, M. M. *et al.* Thalamic nuclei convey diverse contextual information to layer 1 of visual cortex. *Nat. Neurosci.* **19,** 299–307 (2016).
42. Bryan, W. P. & Byrne, R. H. A calcium chloride solution, dry-ice, low temperature bath. *J. Chem. Educ.* **47,** 361 (1970).
43. Morris, J., Singh, J. M. & Eberwine, J. H. Transcriptome analysis of single cells. *J. Vis. Exp.* **50,** e2634 (2011).

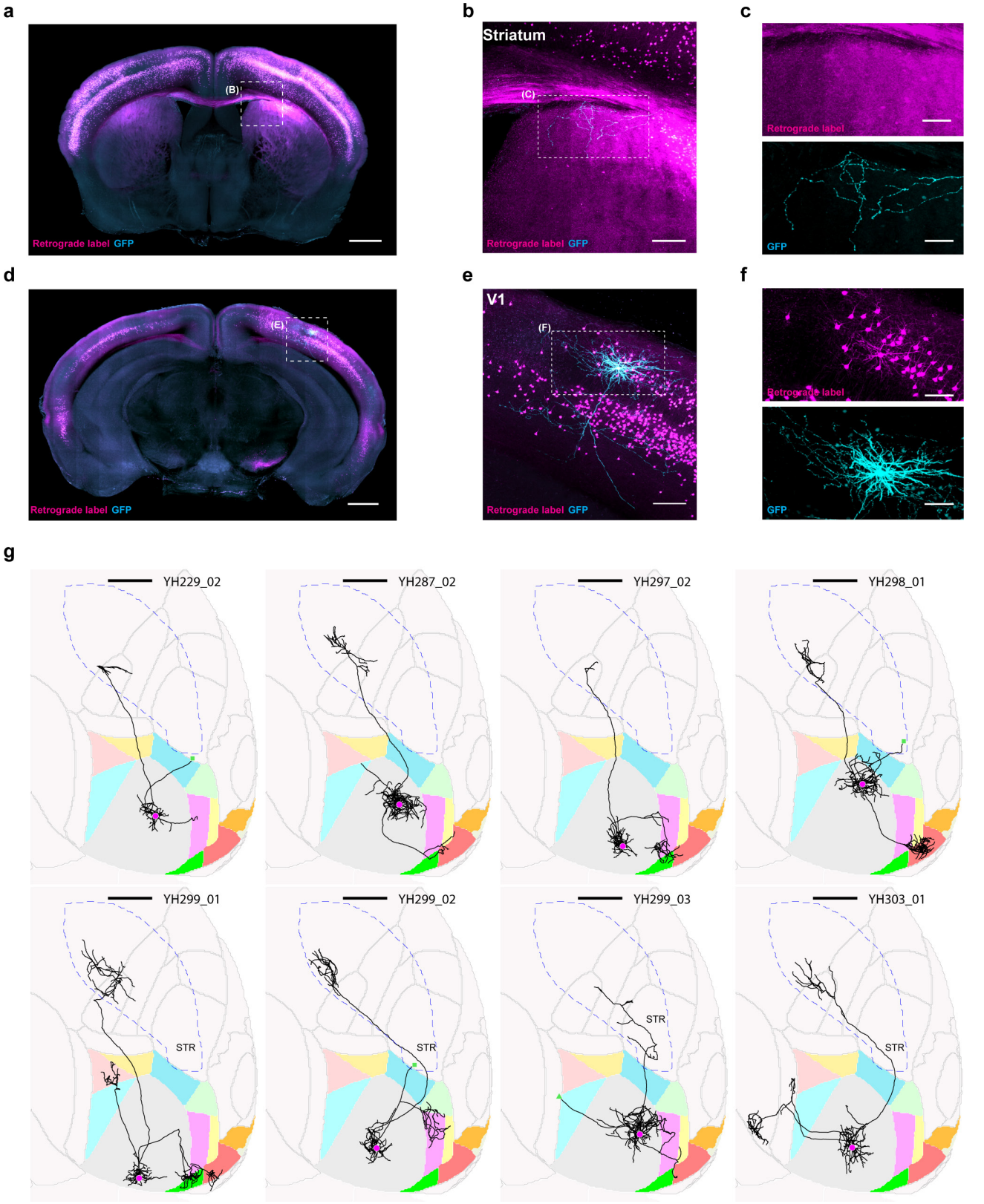

Extended Data Figure 1 | Single-neuron tracing protocol efficiently fills axons projecting to the ipsilateral striatum. We retrogradely labelled striatum-projecting cells by stereotactically injecting cholera toxin subunit B conjugated to AlexaFluor 594 or PRV-Cre into the visual striatum of wild-type mice or tdTomato-reporter mice (Ai14, Jax), respectively (magenta). With visual guidance of two-photon microscopy, we electroporated single retrogradely labelled cells in V1 with a GFP-expressing plasmid (cyan). **a**, Coronal, maximum intensity projections of visual striatum. Scale bar, 1 mm. **b**, Higher magnification image of the visual striatum. Scale bar, 0.2 mm. **c**, Single-channel images of the same axonal arborization as in **b**. **d**, Coronal maximum intensity projection containing V1. Scale bar, 1 mm. **e**, Higher magnification image of V1. Scale bar, 0.2 mm. **f**, Single-channel images of V1. Scale bars, 0.2 mm. **g**, Horizontal projections in the Allen Reference Atlas space of eight retrogradely labelled and electroporated cells. Cell ID numbers are indicated at the top right of each image. Scale bars, 1 mm. Note that one additional cell was retrogradely labelled and electroporated, which revealed its axonal projection to the striatum, but it is not shown because the brain was too distorted to allow accurate registration to the Allen Reference Atlas.

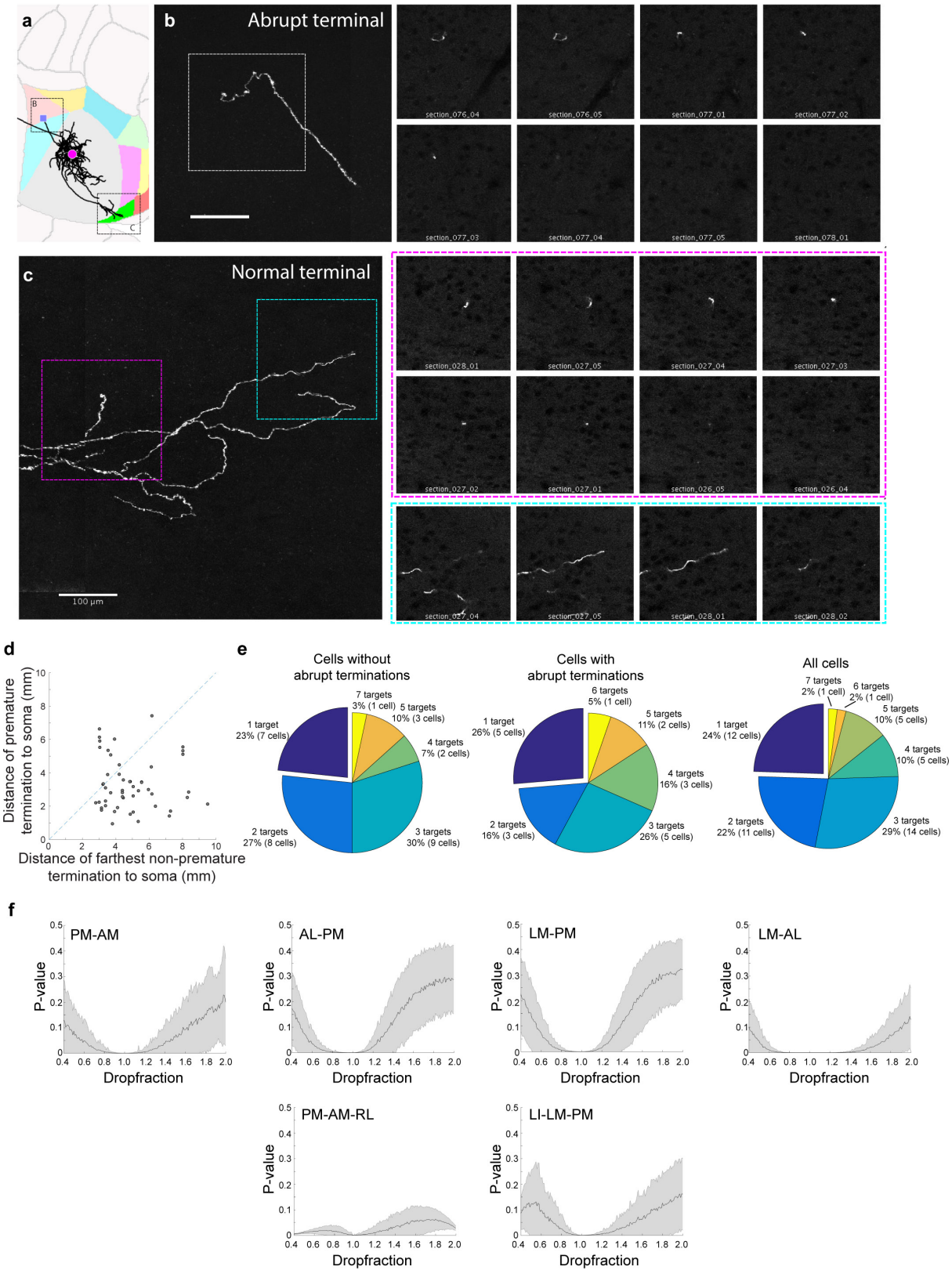

Extended Data Figure 2 | See next page for caption.

Extended Data Figure 2 | Some axonal branches terminate abruptly without arborizing, whereas other branches of the same neuron arborize extensively within different target areas and appear to be completely filled. a, Horizontal view of a representative cell in the Allen Reference Atlas space. The abrupt termination is labelled with a purple square. $n = 28$ abruptly terminating cells. **b**, The abrupt termination of the example cell shown as a maximum z projection (left) and in the individual z sections (right). **c**, Two normal terminations of the same cell, shown as a maximum z projection (left) and in two colour-coded series of z sections (right). **d**, Distance of abrupt termination from cell body versus distance of furthest regular termination of the same cell. Dashed line indicates the unity line. **e**, The distribution of target numbers of all projection neurons without abrupt terminations (as shown in the main figures; left), of projection cells with abrupt terminations (middle) and of all projection neurons (no abrupt terminations and abrupt terminations; right). **f**, To test the effect of false negatives on our analyses, we simulated the random loss or gain of projections from the MAPseq dataset, while maintaining overall area projection probabilities. $n = 553$ neurons; 400 repeats. P values based on a binomial test for all six projection motifs determined as significantly over- or underrepresented in our dataset are plotted after removing (dropfraction <1) or adding (dropfraction >1) connections. Mean (black line) and s.d. (shaded area) are indicated.

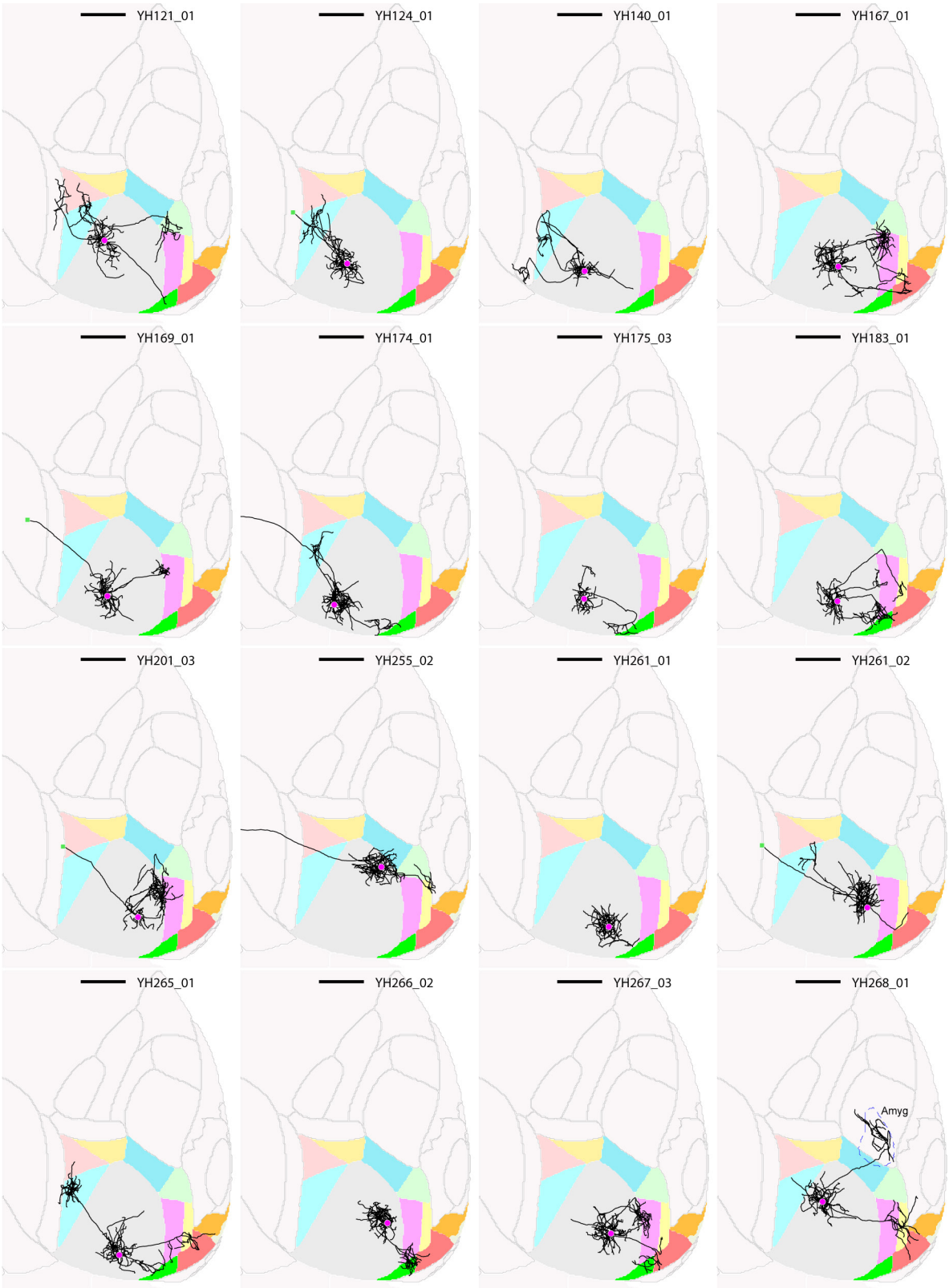

Extended Data Figure 3 | Images of traced layer-2/3 V1 neurons. Horizontal views of the Allen Reference Atlas space are shown, and cell ID numbers are indicated at the top right of each image. Scale bars, 1 mm.

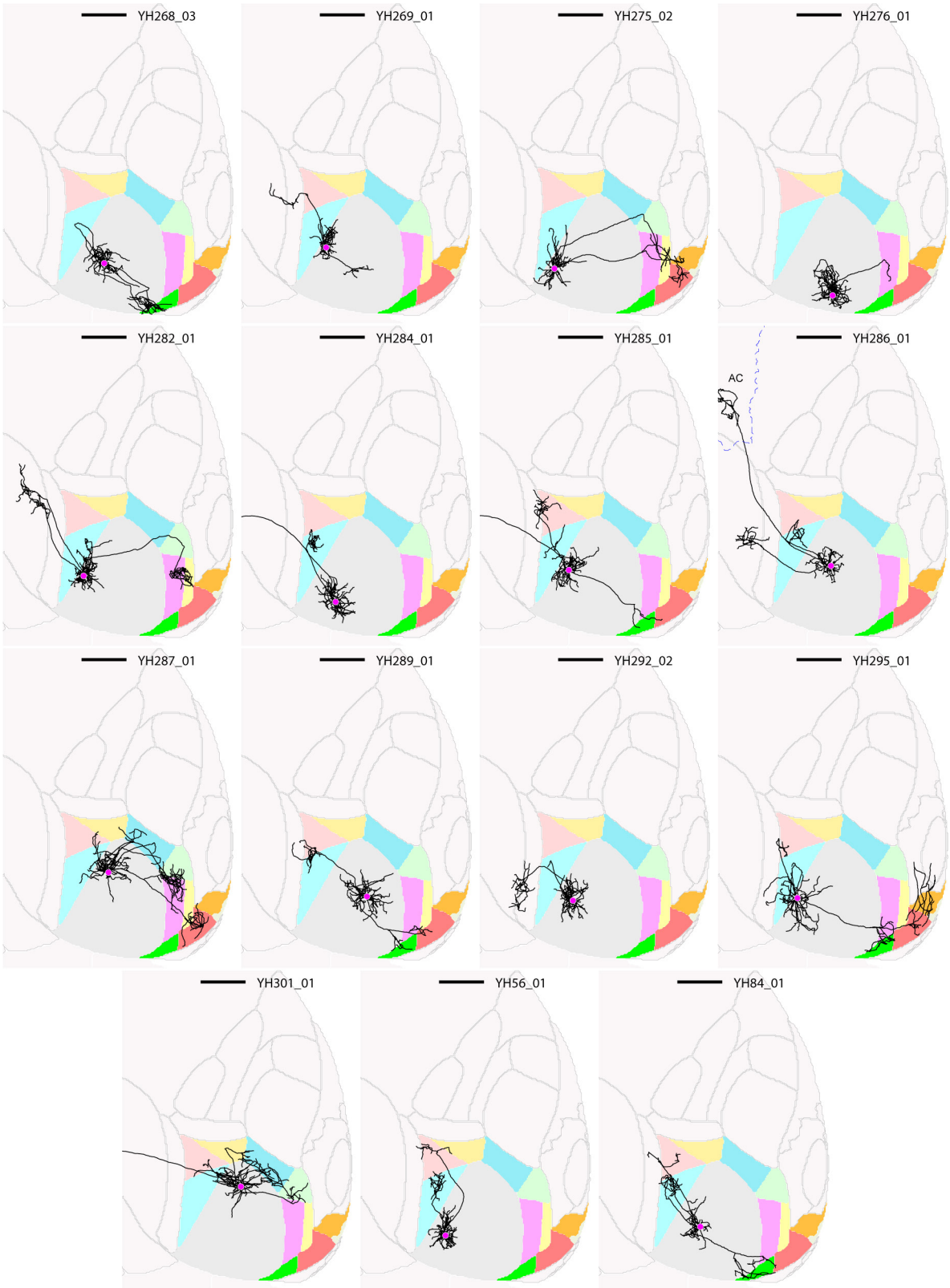

Extended Data Figure 4 | Images of traced layer-2/3 V1 neurons, continued. Horizontal views of the Allen Reference Atlas space are shown, and cell ID numbers are indicated at the top right of each image. Scale bars, 1 mm.

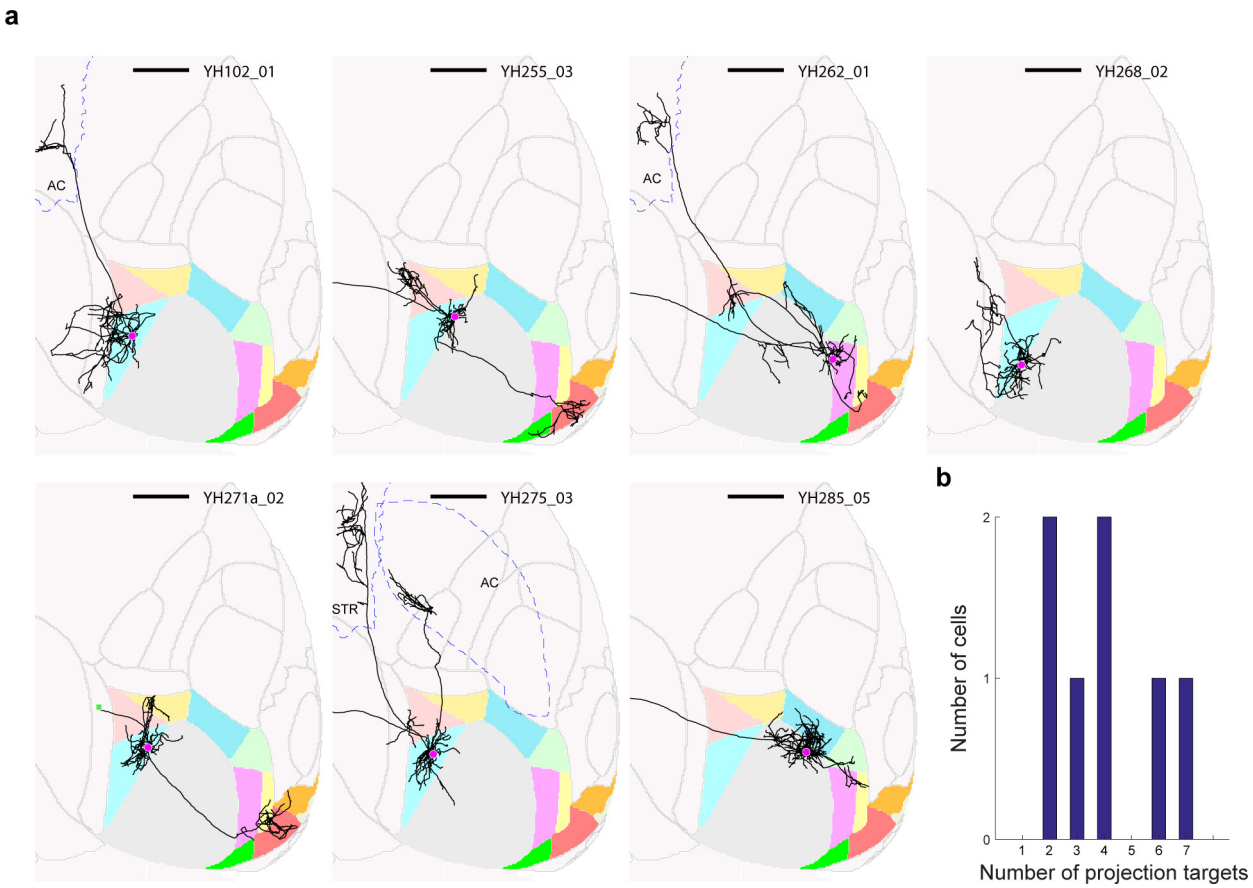

Extended Data Figure 5 | Individual neurons in higher visual areas project to more than one target area. a, All traced neurons with cell bodies not in V1. Brain area identity is colour coded as in Fig. 1. Cell identity is indicated at the top right of each image. Scale bars, 1 mm. **b**, Histogram of the number of target areas per cell.

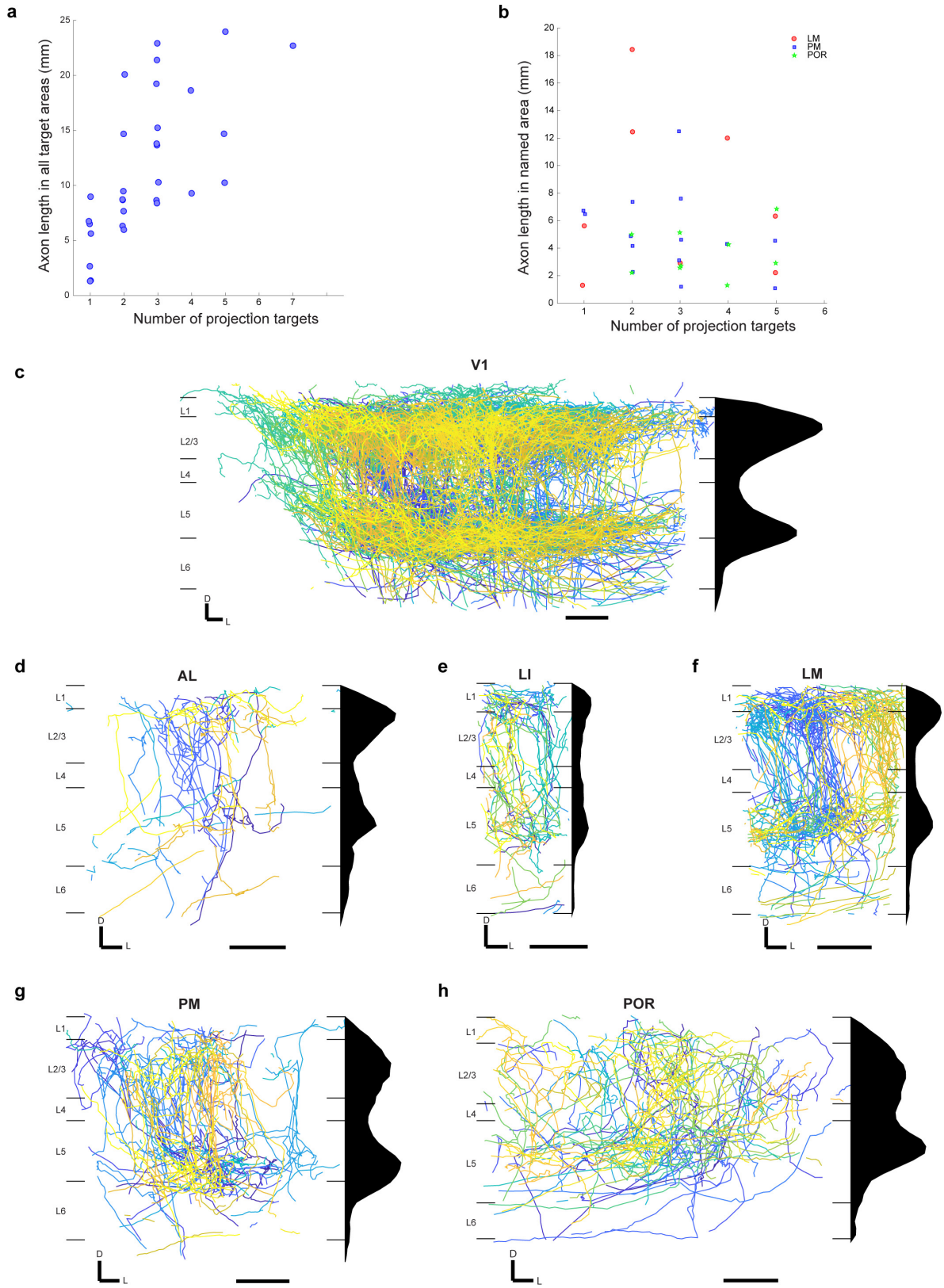

Extended Data Figure 6 | Density of axonal innervation by area and layer of V1 layer-2/3 projection neurons. a, Total axon length plotted as a function of the number of targets innervated by every V1 projection neuron. **b**, Axon length in area LM, PM or POR plotted as a function of the total number of targets innervated by each neuron projection to the respective area. **c**–**h**, The axons of V1 neurons in target areas most densely innervate layers 2/3 and 5, with some density in layer 1, but less in layers 4 and 6, often recapitulating the laminar axonal profile within V1. Coronal views of each area are shown in Allen Reference Atlas space (left) and axonal arborizations of each neuron innervating the area are colour coded. Scale bars, 200 μm. A histogram of the laminar innervation is shown (right). Note that cells with abrupt terminations outside the shown area were included in this analysis. Areas depicted are V1 (**c**), AL (**d**), LI (**e**), LM (**f**), PM (**g**) and POR (**h**). White-matter axons are not shown.

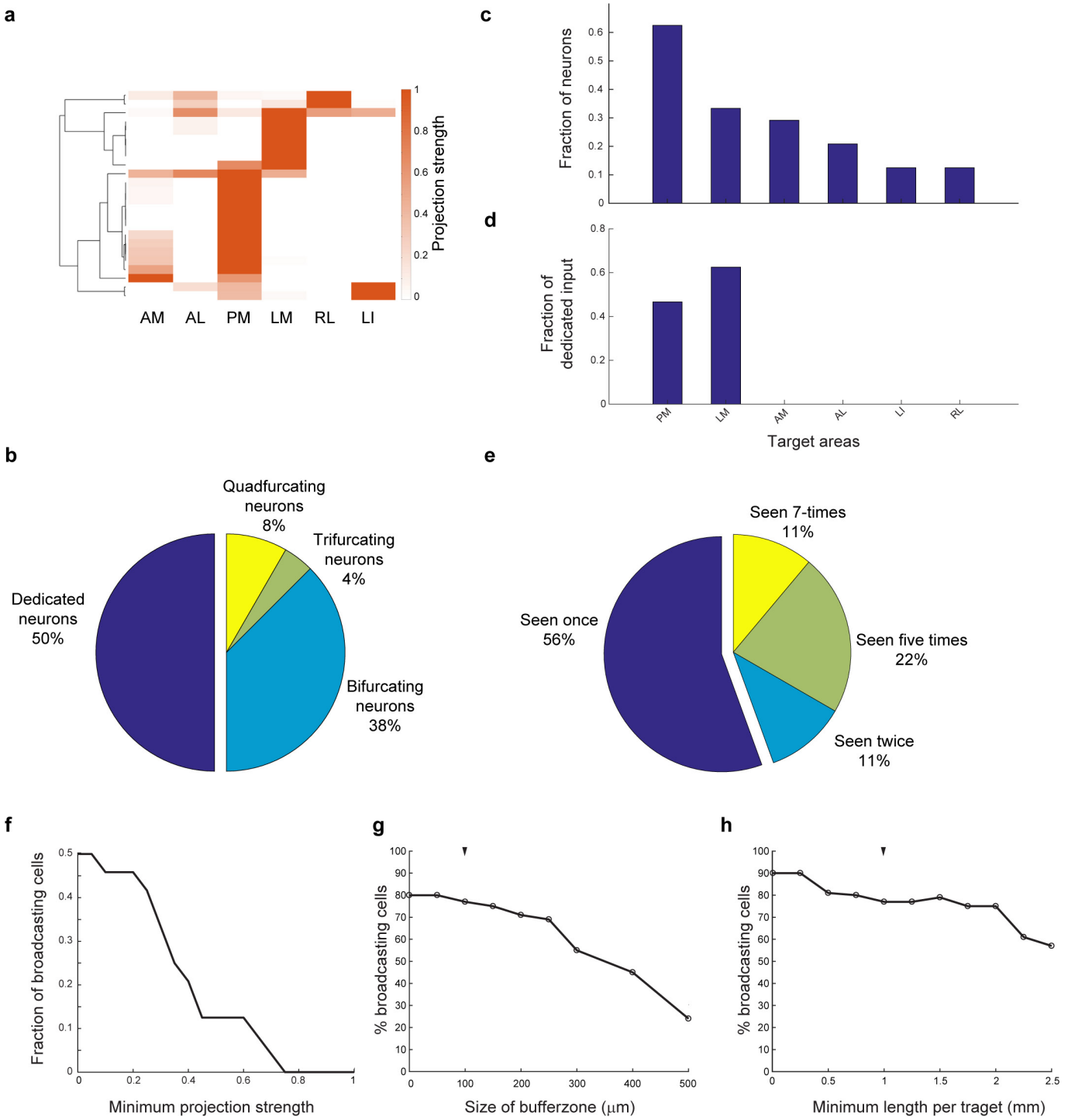

Extended Data Figure 7 | Conclusions from fluorescence-based single-neuron tracing data hold true when the analysis is restricted to subset of target areas. a, The projection patterns of reconstructed GFP-filled neurons when only the six target areas (LI, LM, AL, PM, AM and RL) are considered. Projection strengths are normalized to the maximum projection of each neuron, and only neurons projecting to at least one target area are shown. **b**, The distribution of target area numbers per projection neuron. **c**, The fraction of all cells projecting to each target area. **d**, The fraction of dedicated input per area. **e**, The number of times each binarized projection motif is observed. **f**, The fraction of broadcasting cells as a function of the minimum projection strength (relative to the primary target) that each area needs to receive to be considered a target. **g**, The fraction of broadcasting cells as a function of increasing buffer zones between areas within which axons are ignored, assuming a minimum projection of 1 mm of axon per target area. **h**, The fraction of broadcasting cells as a function of the minimal amount of axon per area for it to be considered a target, assuming buffer zones of 100-μm width. Black arrowheads indicate chosen buffer zones and minimal projection for analysis in the paper.

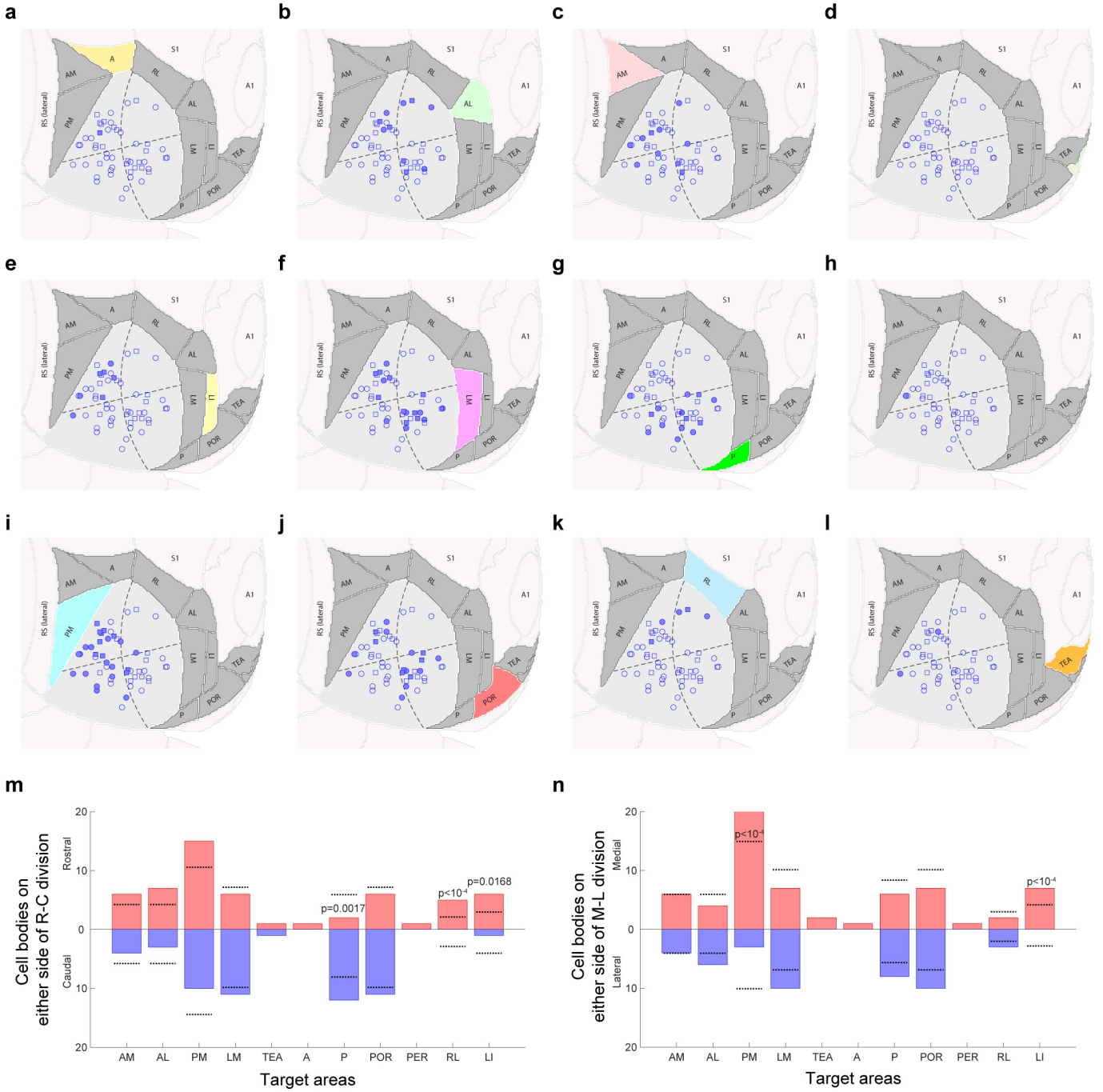

Extended Data Figure 8 | Location of cell bodies in V1 as a function of their projection targets. a–l, Horizontal views of Allen Reference Atlas space are shown. The location of all traced V1 neurons are indicated as circles (cells with no abrupt terminations) or squares (cells with abrupt terminations). In each plot, the cells projecting to the highlighted higher visual area are coloured in solid blue. Target areas considered are A (**a**), AL (**b**), AM (**c**), ECT (**d**), LI (**e**), LM (**f**), P (**g**), PER (**h**), PM (**i**), POR (**j**), RL (**k**) and TEA (**l**). **m**, **n**, Quantification of cell body location in the rostrocaudal (**m**) and mediolateral (**n**) direction. Dotted lines indicate expected number of cells based on a bootstrapping procedure, for which we randomly selected neurons from the available positions to project to each area and repeated the process 10,000 times. *P* values were derived from the bootstrapping probability distribution and are indicated for projection targets significantly deviating from this expectation ($\alpha = 0.05$). *P* values below 10^{-4} are not exact and are therefore indicated as a range.

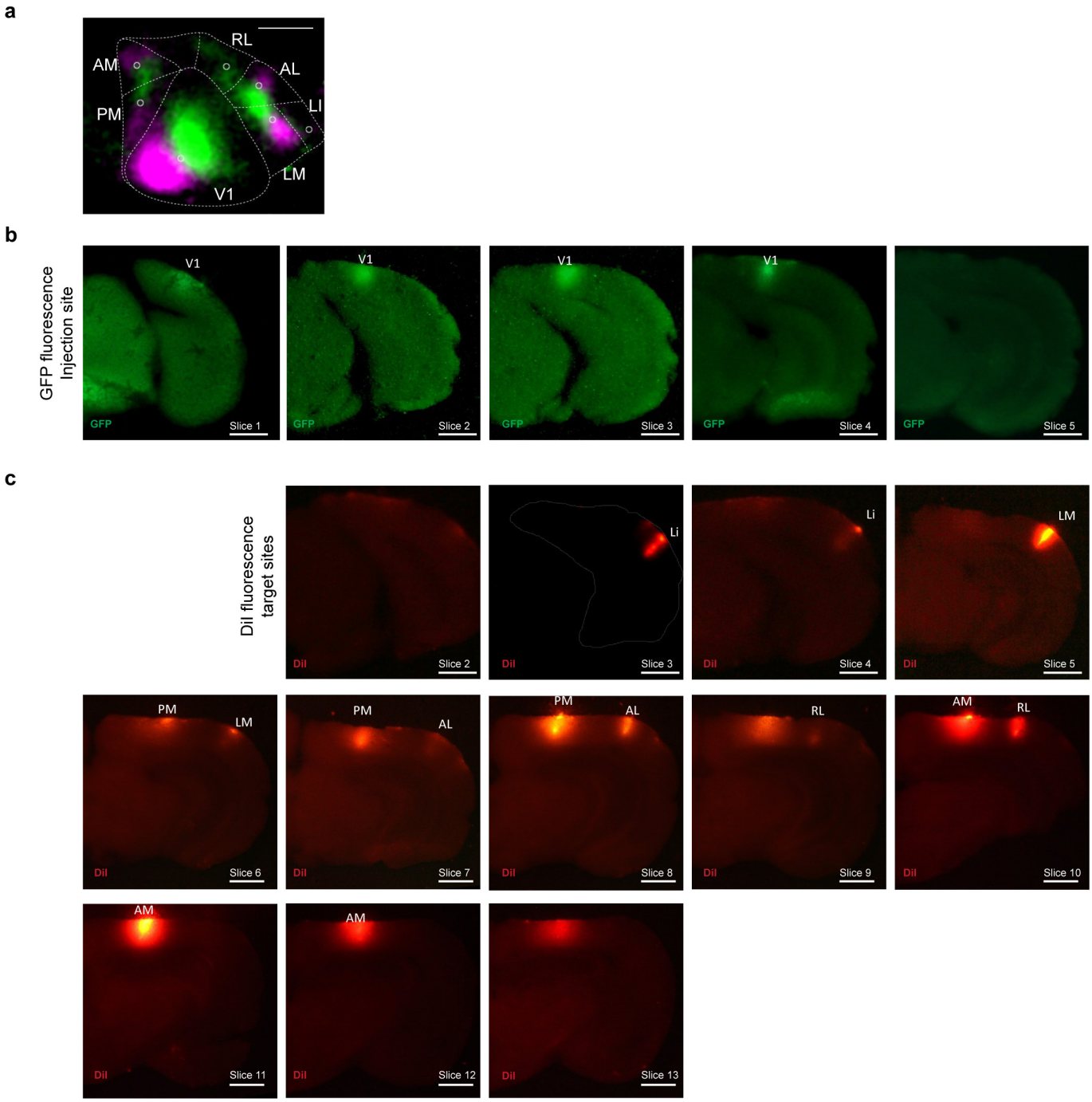

Extended Data Figure 9 | MAPseq dissection strategy. We identified the to-be-dissected higher visual areas by performing intrinsic imaging of visual cortex in response to stimuli at different positions in the contralateral visual field and mapping the resulting changes in intrinsic signals. **a**, A representative retinotopic map, with responses to the two 25° visual stimuli pseudocoloured in green and magenta (stimulus 1 position: 90° azimuth, 20° elevation; stimulus 2 position: 60° azimuth, 20° elevation). On the basis of this map, we fluorescently labelled retinotopically matched positions in the to-be-dissected cortical areas with a DiI stab (white circles). Putative borders between the higher visual areas are indicated with dashed lines for orientation. Scale bar, 1 mm. $n = 4$ mice. **b**, The MAPseq virus injection site is discernible in consecutive frozen 180-μm thick coronal sections, using GFP fluorescence. Scale bars, 1 mm. **c**, DiI injections targeted to matched retinotopic positions in six target areas identified by intrinsic signal imaging. DiI epifluorescence images of each 180-μm thick slice are shown, and dissected areas are labelled. Scale bars, 1 mm.

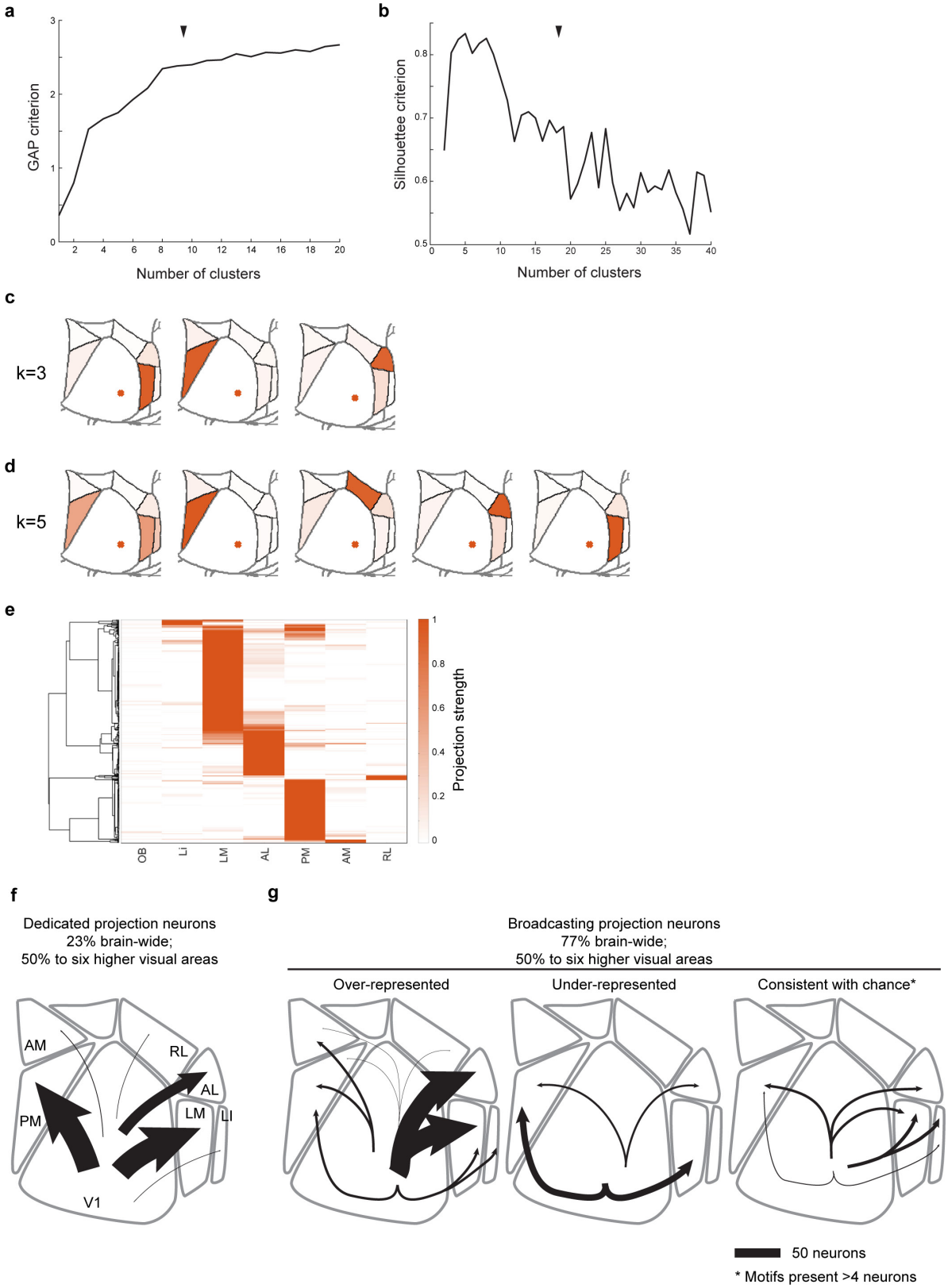

Extended Data Figure 10 | Clustering of MAPseq data and data summary. a, **b**, Gap (**a**) and silhouette criteria (**b**) for *k*-means clustering of the MAPseq neurons as a function of the number of clusters. Black arrow heads indicate chosen number of clusters ($k = 8$). **c**, **d**, Centroids for alternative, near-optimal cluster number choices with $k = 3$ (**c**) and $k = 5$ (**d**). **e**, Hierarchical clustering results of the MAPseq dataset using a cosine distance metric. **c**–**e**, Colour intensity indicates projection strengths. **f**, **g**, Summary of single-neuron projections from V1. **f**, Cells targeting single higher visual areas (dedicated projection neurons) comprise the minority of layer-2/3 V1 projection neurons. Among the areas analysed by MAPseq, dedicated projection neurons predominantly innervate cortical areas LM or PM. **g**, Cells projecting to two or more areas (broadcasting projection neurons) are the dominant mode of information transfer from V1 to higher visual areas. In the six areas analysed by MAPseq, broadcasting neurons innervate combinations of target areas in a non-random manner, including those that are more or less abundant than expected by chance. Line width indicates the absolute abundance of each projection type as observed in the MAPseq dataset.

nature research

Corresponding author(s): Thomas Mrsic-Flogel

Life Sciences Reporting Summary

Nature Research wishes to improve the reproducibility of the work that we publish. This form is intended for publication with all accepted life science papers and provides structure for consistency and transparency in reporting. Every life science submission will use this form; some list items might not apply to an individual manuscript, but all fields must be completed for clarity.

For further information on the points included in this form, see Reporting Life Sciences Research. For further information on Nature Research policies, including our data availability policy, see Authors & Referees and the Editorial Policy Checklist.

Please do not complete any field with "not applicable" or n/a. Refer to the help text for what text to use if an item is not relevant to your study.
For final submission: please carefully check your responses for accuracy; you will not be able to make changes later.

Experimental design

1. Sample size

Describe how sample size was determined.

No sample size calculations were performed.

2. Data exclusions

Describe any data exclusions.

We excluded fluorescence-based reconstructed neurons that showed abrupt terminations in the ipsilateral hemisphere from analysis. Cells with cell bodies in layer 5 of mouse 7 of the MAPseq data were excluded from analysis, as this sample appears t be contaminated by area LM.

3. Replication

Describe the measures taken to verify the reproducibility of the experimental findings.

All findings replicated across animals, subject to the sampling inherent in single cell tracing approaches.

4. Randomization

Describe how samples/organisms/participants were allocated into experimental groups.

Group allocation is not applicable in this study, as we do not compare across treatment conditions but report only static connectivity properties.

5. Blinding

Describe whether the investigators were blinded to group allocation during data collection and/or analysis.

No blinding was used for fluorescence based single neuron reconstructions. The researcher producing the MAPseq sequencing libraries was blinded to sample identity.

Note: all in vivo studies must report how sample size was determined and whether blinding and randomization were used.

6. Statistical parameters

For all figures and tables that use statistical methods, confirm that the following items are present in relevant figure legends (or in the Methods section if additional space is needed).

n/a	Confirmed
☐	☒ The exact sample size (*n*) for each experimental group/condition, given as a discrete number and unit of measurement (animals, litters, cultures, etc.)
☐	☒ A description of how samples were collected, noting whether measurements were taken from distinct samples or whether the same sample was measured repeatedly
☐	☒ A statement indicating how many times each experiment was replicated
☐	☒ The statistical test(s) used and whether they are one- or two-sided *Only common tests should be described solely by name; describe more complex techniques in the Methods section.*
☐	☒ A description of any assumptions or corrections, such as an adjustment for multiple comparisons
☐	☒ Test values indicating whether an effect is present *Provide confidence intervals or give results of significance tests (e.g. P values) as exact values whenever appropriate and with effect sizes noted.*
☐	☒ A clear description of statistics including central tendency (e.g. median, mean) and variation (e.g. standard deviation, interquartile range)
☐	☒ Clearly defined error bars in all relevant figure captions (with explicit mention of central tendency and variation)

See the web collection on statistics for biologists for further resources and guidance.

Software

Policy information about availability of computer code

7. Software

Describe the software used to analyze the data in this study.	All software used to analyses the data in this study are available from GitHub and http://mouse.vision/han2017. This includes custom pipelines for stiching of the 2-photon-tomography imaging data, atlas aligment and single neuron tracing, as well as MAPseq data analysis (extraction of barcode reads from raw sequencing data, error correction, barcode matching and barocode matrix construction) as well as custom analysis code to produce the figures in the manuscript.

For manuscripts utilizing custom algorithms or software that are central to the paper but not yet described in the published literature, software must be made available to editors and reviewers upon request. We strongly encourage code deposition in a community repository (e.g. GitHub). *Nature Methods* guidance for providing algorithms and software for publication provides further information on this topic.

Materials and reagents

Policy information about availability of materials

8. Materials availability

Indicate whether there are restrictions on availability of unique materials or if these materials are only available for distribution by a third party.	All materials used in this study are available from standard commercial sources, or from addgene.org.

9. Antibodies

Describe the antibodies used and how they were validated for use in the system under study (i.e. assay and species).	No antibodies were used in this study.

10. Eukaryotic cell lines

a. State the source of each eukaryotic cell line used.	No eukaryotic cell lines were used in this study.
b. Describe the method of cell line authentication used.	No eukaryotic cell lines were used in this study.
c. Report whether the cell lines were tested for mycoplasma contamination.	No eukaryotic cell lines were used in this study.
d. If any of the cell lines used are listed in the database of commonly misidentified cell lines maintained by ICLAC, provide a scientific rationale for their use.	No eukaryotic cell lines were used in this study.

Animals and human research participants

Policy information about studies involving animals; when reporting animal research, follow the ARRIVE guidelines

11. Description of research animals

Provide all relevant details on animals and/or animal-derived materials used in the study.	male and female adult (>8 weeks of age) C57BL/6 mice

Policy information about studies involving human research participants

12. Description of human research participants

Describe the covariate-relevant population characteristics of the human research participants.	This study did not involve human research participants.